RADIATIVE COOLING

Temperature-adaptive radiative coating for all-season household thermal regulation

Kechao Tang[1,2,3]†, Kaichen Dong[1,2]†, Jiachen Li[2,4]†, Madeleine P. Gordon[4,5], Finnegan G. Reichertz[6], Hyungjin Kim[2,7], Yoonsoo Rho[8], Qingjun Wang[1,2], Chang-Yu Lin[1], Costas P. Grigoropoulos[8], Ali Javey[2,7], Jeffrey J. Urban[5], Jie Yao[1,2], Ronnen Levinson[9], Junqiao Wu[1,2,4]*

The sky is a natural heat sink that has been extensively used for passive radiative cooling of households. A lot of focus has been on maximizing the radiative cooling power of roof coating in the hot daytime using static, cooling-optimized material properties. However, the resultant overcooling in cold night or winter times exacerbates the heating cost, especially in climates where heating dominates energy consumption. We approached thermal regulation from an all-season perspective by developing a mechanically flexible coating that adapts its thermal emittance to different ambient temperatures. The fabricated temperature-adaptive radiative coating (TARC) optimally absorbs the solar energy and automatically switches thermal emittance from 0.20 for ambient temperatures lower than 15°C to 0.90 for temperatures above 30°C, driven by a photonically amplified metal-insulator transition. Simulations show that this system outperforms existing roof coatings for energy saving in most climates, especially those with substantial seasonal variations.

In countries such as the United States, ~39% of the total energy consumption is in buildings (*1*). For the residential housing energy portion, ~51% is consumed for heating and cooling to maintain a desirable indoor temperature (~22°C) (*2*). In contrast to most temperature regulation systems, which require external power input, the mid-infrared (IR) atmospheric transparency window ("sky window") allows thermal radiation exchange between terrestrial surfaces and the 3 K outer space, thus opening a passive avenue for thermal radiative cooling of buildings. This method to cool an outdoor surface such as a roof has been extensively studied in the past (*3*–*6*). It is now advanced by the development of daytime radiative cooling (*7*–*13*) using materials with low solar absorptance and high thermal emittance in the form of thin films (*8*), organic paints (*10*, *14*), or structural materials (*11*).

Past research on daytime radiative cooling, while successful in reducing cooling energy consumption, typically used materials with fixed, cooling-optimized properties, which efficiently emit thermal radiation even when the temperature of the surface is lower than desired, such as during the night or in the winter. This unwanted thermal radiative cooling will increase the energy consumption for heating and may offset the cooling energy saved in hot hours or seasons. This issue is well acknowledged by the research community, and mitigation of the overcooling has become a timely demand (*15*). To cut the heating penalty from overcooling, a few techniques were recently attempted for switching off thermal radiative cooling at low temperatures (below 22°C). Although effective in switching, these techniques typically require either additional energy input (*16*, *17*) or external activation (*18*), and in some cases, switching is achieved by mechanical moving parts (*19*, *20*). Developing dynamic structures that automatically cease radiative cooling at low temperatures is therefore highly desirable. Existing efforts in self-switching radiative cooling, however, are either purely theoretical (*21*–*24*) or limited to materials characterization with little relevance to practical household thermal regulation (*25*–*28*). Very recently, a smart subambient coating was developed (*29*), focusing on the reduction of solar absorption by fluorescence rather than modulation of thermal emittance by temperature.

We took a different, holistic approach by designing and fabricating a mechanically flexible coating structure to minimize total energy consumption through the entire year. This temperature-adaptive radiative coating (TARC) automatically switches its sky-window emittance to 0.90 from 0.20 when the surface temperature rises above ~22°C, a practical threshold not previously available. Our TARC delivers high radiative cooling power exclusively for the high-temperature condition (Fig. 1A). We also optimized the solar absorptance at ~0.25 (solar reflectance = 0.75) for all-season energy saving in major US cities (fig. S7). Our TARC demonstrates effective surface temperature modulation in an outdoor test environment. We performed extensive simulations based on the device properties and the climate database, which show advantages of TARC over existing roof coating materials in energy savings for most US cities in different climate zones (Fig. 1C). The energy savings by TARC not only bring economic benefits but also contribute to environmental preservation by reducing greenhouse gas emissions.

We developed the TARC based on the well-known metal-insulator transition (MIT) of the strongly correlated electron materials $W_xV_{1-x}O_2$ (*30*–*32*), and the transition temperature (T_{MIT}) is tailored to ~22°C by setting the composition x at 1.5% (*33*). We embedded a lithographically patterned two-dimensional array of thin $W_xV_{1-x}O_2$ blocks in a BaF_2 dielectric layer that sits on top of an Ag film (Fig. 2A). In the insulating (I) state of $W_xV_{1-x}O_2$ at $T < T_{MIT}$, the material is largely transparent to the infrared (IR) radiation in the 8- to 13-μm sky spectral window, so this sky-window IR radiation is reflected by the Ag mirror with little absorption (*34*). By contrast, the $W_xV_{1-x}O_2$ becomes highly absorptive in the sky window when it switches to the metallic (M) state at $T > T_{MIT}$ (*34*). The absorption is further amplified by the designed photonic resonance with adjacent $W_xV_{1-x}O_2$ blocks as well as with the bottom Ag layer through the ¼-wavelength cavity. The ¼-wavelength cavity structure induces Fabry-Perot resonance and was used in previous work to enhance thermal emission (*21*, *23*). According to Kirchhoff's law of radiation (*35*), the sky-window emittance equals the sky-window absorptance and switches from low to high when the temperature exceeds T_{MIT}. Consequently, strong sky-window radiative cooling is turned on in operation exclusively at high temperatures, leaving the system in the solar-heating or keep-warm mode at low temperatures. Details on the fabrication process and structural parameters are found in the supplementary materials (*36*) (fig. S1).

Our fabricated TARC has high flexibility for versatile surface adaption, as well as a micro-scale structure consistent with the design (Fig. 2B). We examined the emittance switching over the entire sample using a thermal infrared (TIR) camera (Fig. 2C). We imaged the TARC surface together with two reference samples having similar thicknesses but constant low thermal emittance (0.10, copper plate) or constant high thermal emittance (0.95, black tape), respectively. Although the thermal emission of the reference samples appeared to not be strongly temperature sensitive from 20 to 30°C, the TARC showed a marked change, corresponding to the switch in sky-window emittance at the MIT around 22°C.

[1]Department of Materials Science and Engineering, University of California, Berkeley, CA 94720, USA. [2]Materials Sciences Division, Lawrence Berkeley National Laboratory, Berkeley, CA 94720, USA. [3]Key Laboratory of Microelectronic Devices and Circuits (MOE), School of Integrated Circuits, Peking University, Beijing 100871, P. R. China. [4]Applied Science and Technology Graduate Group, University of California, Berkeley, CA, 94720, USA. [5]The Molecular Foundry, Lawrence Berkeley National Laboratory, Berkeley, CA 94720, USA. [6]East Bay Innovation Academy, 3800 Mountain Blvd., Oakland, CA 94619, USA. [7]Department of Electrical Engineering and Computer Sciences, University of California, Berkeley, CA 94720, USA. [8]Department of Mechanical Engineering, University of California, Berkeley, CA 94720, USA. [9]Heat Island Group, Lawrence Berkeley National Laboratory, Berkeley, CA 94720, USA.
*Corresponding author. Email: wuj@berkeley.edu
†These authors contributed equally to this work.

We measured the spectral properties of the TARC by a UV-visible-NIR spectrometer and Fourier transform infrared spectroscopy (FTIR) for the solar and TIR wavelength regimes, respectively (Fig. 2D). The solar absorptance (A, 0.3 to 2.5 μm) is ~0.25, and the sky-window emittance (ε_w, 8 to 13 μm) is ~0.20 in the I state and ~0.90 in the M state, consistent with theoretical simulations and other characterization results (fig. S2 and fig. S3).

The emittance switching of the TARC enables deep modulation of radiative cooling power in response to ambient temperature, which we first measured in vacuum (Fig. 3A). We suspended a heater membrane by thin strings in a vacuum chamber, which was cooled with dry ice to ~−78°C to minimize radiation from the chamber walls. We attached a piece of Al foil with $\varepsilon_{Al} \approx 0.03$ or a TARC of the same size to the top of the heater in two separate measurements. At each stabilized sample temperature T, the heating powers needed for the two coating scenarios are denoted as $P_{Al}(T)$ and $P_{TARC}(T)$, respectively. The cooling flux (power per area $\mathcal{A}$) contributed by the TARC was calculated as $P''_{cool}(T) = [P_{TARC}(T) - P_{Al}(T)]/\mathcal{A}$. We used the Al foil reference to calibrate background heat loss from thermal conduction through the strings. We plotted the calibrated cooling power (Fig. 3B), which shows an abrupt increase in $P''_{cool}(T)$ when T rises above the MIT temperature. $P''_{cool}(T)$ measurements in the I state and M state are well fitted by the Stefan-Boltzmann radiation law, with values of sky-window ε_w extracted to be ~0.20 and ~0.90, respectively, consistent with the spectrally characterized results (Fig. 2D). We considered and corrected the effect of radiation from the chamber wall (~−78°C) for the calibration. We introduced a constant factor of γ (≈ 0.7) to account for the difference between the vacuum and ambient measurement conditions (details in fig. S4) (*36*).

We demonstrated the actual outdoor performance of the TARC (Fig. 4). We recorded the surface temperatures (T_s) of the TARC, together with a dark roof coating product (Behr no. N520, asphalt gray) and a cool (white) roof coating product (GAF RoofShield white acrylic), over 24 hours on a sunny summer day on a rooftop in Berkeley, California, with a careful design of the measurement system to minimize the effects of artifacts (fig. S5).

From 00:00 to 09:00 local daylight time (LDT), when the ambient temperature was below T_{MIT}, the TARC was 2°C warmer than the two reference roof coatings, arising from the low sky-window emittance ($\varepsilon_w = 0.20$) of the TARC in the I state and thus a lower radiative cooling power than the references ($\varepsilon_w = 0.90$). The 2°C temperature elevation is consistent with adiabatic simulation results based on these nominal emittance values and the local weather database [see the supplementary materials (*36*), note A, section I]. From 09:00 to 13:00 LDT, when the samples were in direct sunlight, T_s was dominated by the solar absorption in balance with radiative cooling and air convection, and the differences between the samples agree with the simulated results assuming the solar absorptance A to be 0.15, 0.25, and 0.70 for the white roof coating, TARC, and the dark roof coating, respectively. After 13:00 LDT, we erected a shield to intentionally block direct solar radiation to the surface of the samples. This imitates the scenario of a cloud blocking the sun but with the rest of the sky mostly clear. We quickly observed a convergence of the T_s curves for all three samples, an indication that the thermal emittance of the TARC in the M state is close to that of the two references (0.90). This condition persisted for a few hours until T_s started to drop below T_{MIT} = 22°C. After this point, TARC grew warmer than the two references, with a final temperature difference of ~2°C, similar to the 00:00 to 09:00 LDT period. This indicates that the TARC switched to the low-emittance I state. The 24-hour outdoor experiments demonstrate the emittance switching and resultant temperature regulation by TARC. Although the white roof coating shows an advantage over TARC in thermal management in summer daytime and under solar radiation (Fig. 4A), the TARC regulates the roof temperature closer to the heating and cooling setpoints (22 and 24°C) than the white roof coating for almost all of the other conditions, including daytime in other seasons and all of the nighttime (fig. S6). From an all-year-round perspective, the TARC demonstrates superiority compared with regular roof coatings in terms of source energy saving.

To directly compare their ambient condition cooling fluxes (P''_{cool_amb}), we heated the TARC and the white roof coating to the air temperature with the direct solar radiation

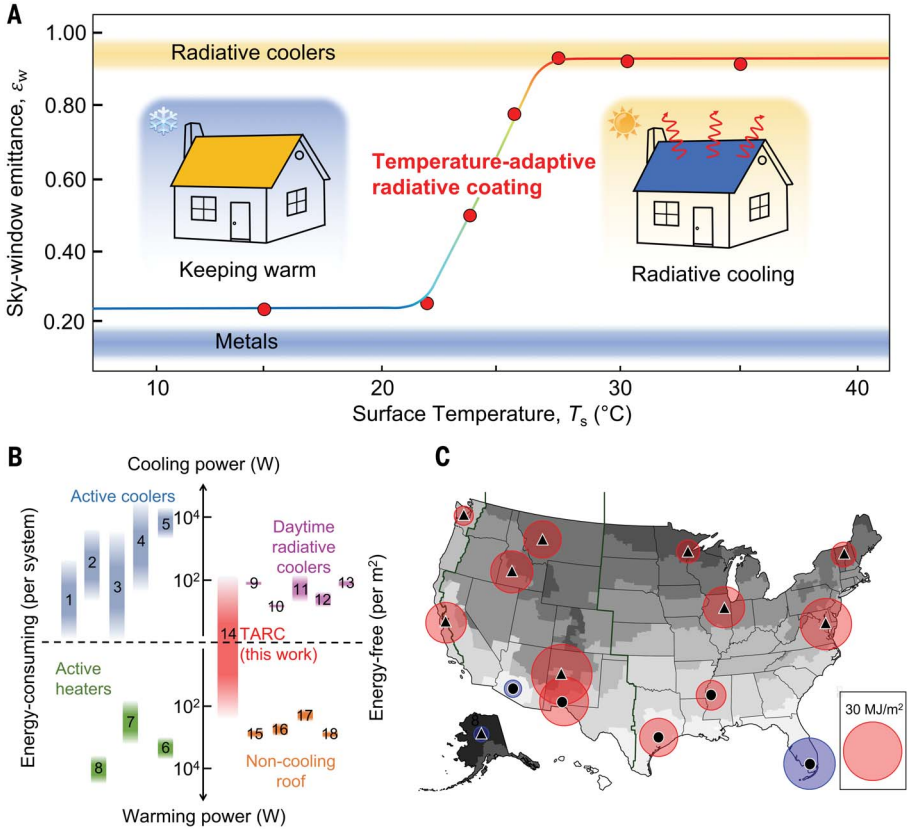

Fig. 1. TARC and its benefits for household thermal regulation. (**A**) Basic property of TARC in sky-window (8 to 13 μm) emittance modulation and schematics for temperature management when used as a household roof coating. The data points are the measured sky-window emittances of a TARC. The two color bands represent the temperature-independent thermal emittance of metals and radiative coolers. (**B**) TARC compared with other thermal regulation systems, highlighting the unique benefit of TARC of being simultaneously energy-free and temperature adaptive (details in table S1). (**C**) $SCSES_{min}$ of TARC compared with other existing roof-coating materials for different cities representing the 15 climate zones in the United States. Red and blue circles indicate positive and negative $SCSES_{min}$ values, respectively. The values are scaled to the area of the circles. Representation of the triangle and circle icons is explained in the materials and methods (subsection, "Projection of energy savings") (*36*).

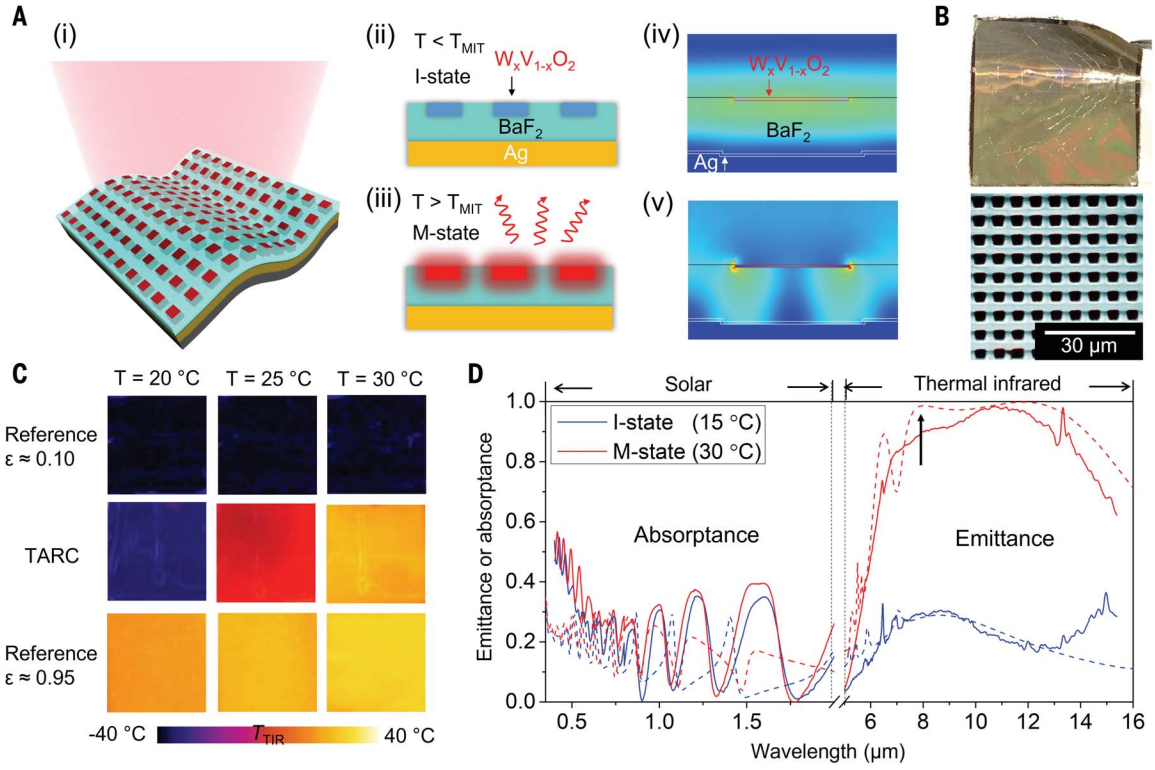

Fig. 2. Basic properties of TARC with experimental characterization. (**A**) Schematics of the structure (i), materials composition and working mechanism (ii and iii) of the TARC. Subpanels (iv) and (v) show the simulated distribution of electric field intensity below and above the transition temperature, respectively, when electromagnetic waves with a wavelength of 7.8 μm were normally incident on the TARC structure. (**B**) Photograph (2 cm × 2 cm) and false-color scanning electron microscope image of TARC showing high flexibility and structural consistency with the design. (**C**) TIR images of TARC compared with those of two conventional materials (references) with constantly low or high thermal emittance showing the temperature-adaptive switching in thermal emittance of TARC. (**D**) Solar spectral absorptance and part of the thermal spectral emittance of TARC at a low temperature and a high temperature, measured by a UV-visible-NIR spectrometer with an integrating sphere and an FTIR spectrometer, respectively. Measurements (solid curves) show consistency with theoretical predictions (dashed curves). The arrow at 7.8 μm denotes the wavelength where the distribution of electric field intensity shown in subpanels (iv) and (v) of (A) are simulated.

blocked. P''_{cool_amb} refers to the net cooling flux from the surface—namely, the thermal radiative heat loss flux minus the absorbed diffuse solar irradiance. We plotted the P''_{cool_amb} values that we obtained at a low and a high air temperature (Fig. 4B). The TARC exhibits a clear switching of P''_{cool_amb} by a factor over five across the MIT. This behavior is in stark contrast to the nearly constant P''_{cool_amb} around 120 W/m^2 for the shaded white roof coating, which is consistent with values (90 to 130 W/m^2) reported in literature for roofs surfaced with daytime radiative cooling materials (*5*, *9*, *10*).

We performed extensive numerical simulations to analyze the performance of TARC in household energy saving for the US cities from an all-season perspective (*36*). We show the simulated results (Fig. 4C) for Berkeley where the measurements (Fig. 4, A and B) were performed. We calculated an hour-month map of T_s using a local weather file (*37*), laying the basis for estimation of energy saving. We assumed heating and cooling setpoints $T_{set,heat}$ = 22°C and $T_{set,cool}$ = 24°C (*38*), and approximated that the building will need heating when $T_s < T_{set,heat}$ and require cooling when $T_s > T_{set,cool}$. We used past simulations of cool-roof energy savings to predict potential space-conditioning source energy savings (SCSES) per unit roof area attainable by using TARC in place of roofing materials that have static values of solar absorptance and thermal emittance (*36*). The figure of merit of TARC is represented by $SCSES_{min}$, the minimum value of SCSES found over all existing conventional roofing materials, which have constant values of A_{ref} and ε_{ref} (Fig. 4C, dashed boxes). We mapped $SCSES_{min}$ for cities representing the 15 US climate zones (Fig. 1C). This figure-of-merit map shows that TARC provides clear, positive annual space-conditioning source energy savings relative to existing roof coating materials in most major cities, except for climates that are constantly cold (such as Fairbanks) or hot (such as Miami) throughout the year. It highlights the advantage of TARC, especially in climate zones with wide temperature variations, day to night or summer to winter. For example, we estimate that for a single-family home in Baltimore, Maryland, built before 1980, modeled with roof assembly thermal insulance 4.3 m^2/(K·W), gas furnace annual fuel utilization efficiency 80%, and air conditioner coefficient of performance 2.64 (*38*), $SCSES_{min}$ is 22.4 MJ/(m^2·y), saving 2.64 GJ/y based on a roof area of 118 m^2. We also calculated the source energy saving of TARC as a function of its solar absorptance (fig. S7), showing that the actual solar absorptance of TARC is close to the optimal value for major US cities.

The TARC could be readily upgraded for heavy-duty outdoor applications by coating it with a thin polyethylene (PE) membrane, which is nontoxic, hydrophobic, and transparent both in the visible and thermal IR regions. While protecting the TARC from contacting the dust and moisture in complex environments, the PE coating has little impact on the thermal modulation performance (fig. S9). Polymer imprinting instead of photolithography could also be used to more easily produce the material for large scale application. By embedding VO_2 particles in layered PE

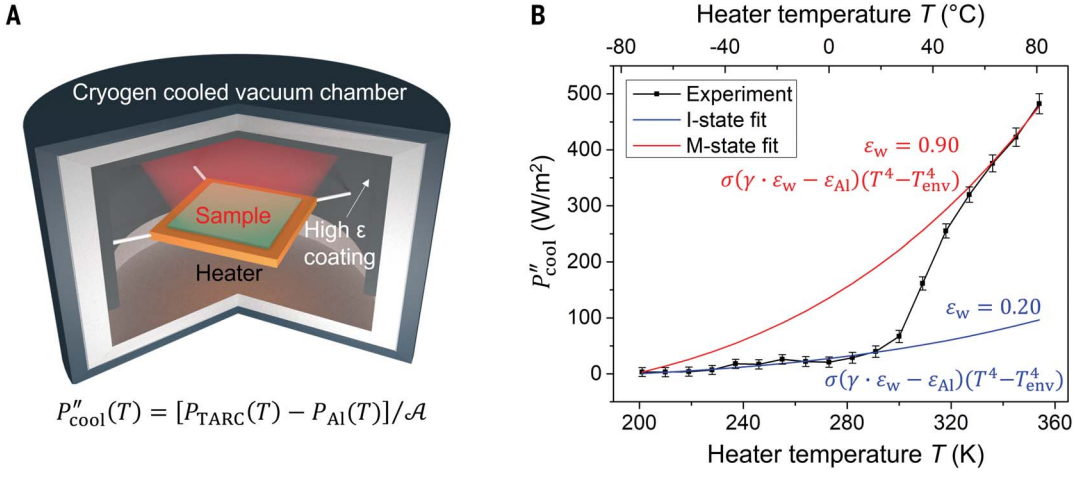

Fig. 3. Characterization of intrinsic radiative cooling power of TARC in a cryogenic vacuum chamber. (**A**) Schematics of the experimental setup showing a thin heater membrane covered by either a TARC or an Al foil and suspended in a cryogen-cooled vacuum chamber. The Al foil reference is used to cancel the effect of thermal loss through conduction. (**B**) Calibrated experimental cooling flux (power/area) of TARC as a function of temperature in vacuum (the black data line). Fitting of $P''_{cool}(T)$ at I and M states by the Stefan-Boltzmann radiation law gives ε_w values of 0.20 and 0.90, respectively.

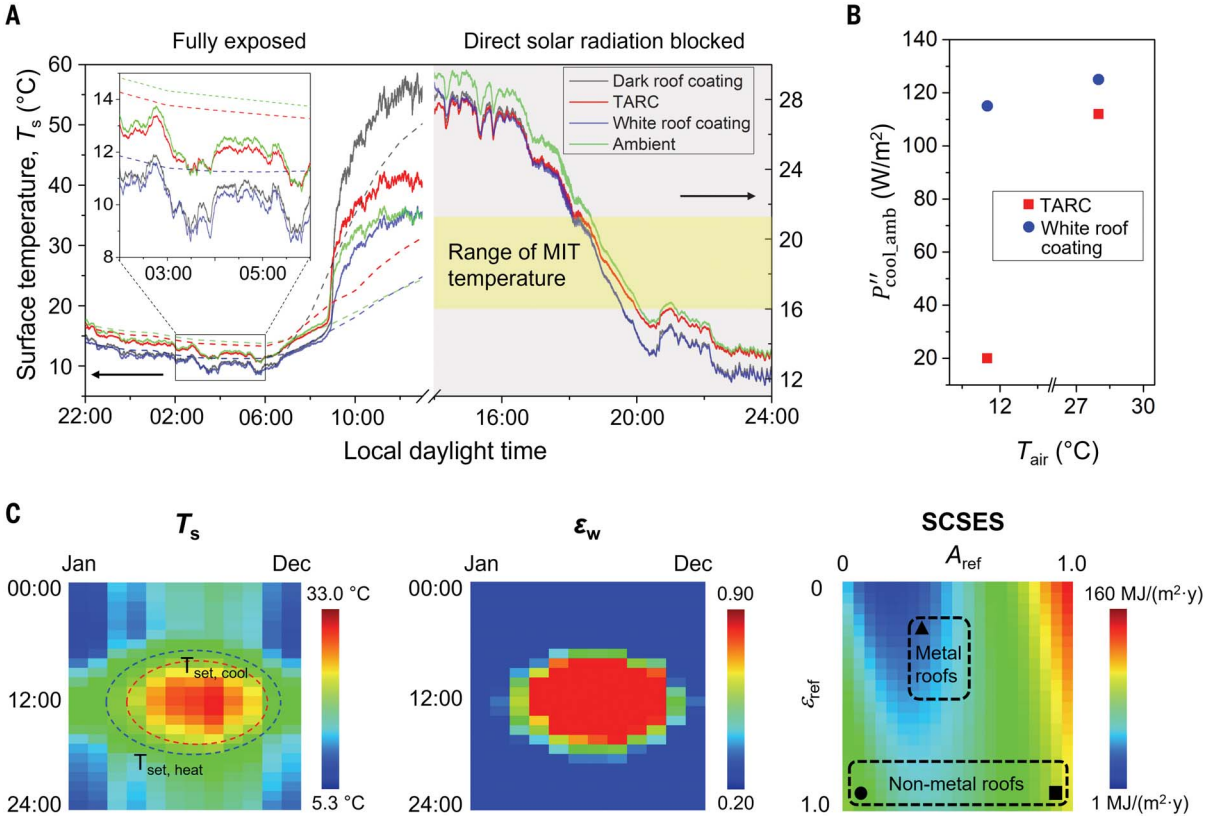

Fig. 4. Characterization of TARC in an outdoor environment. (**A**) Surface temperature of TARC, a commercial dark roof coating (A = 0.70, ε_w = 0.90), and a commercial white roof coating (A = 0.15, ε_w = 0.90) in an open-space outdoor environment recorded over a day-night cycle. The measurement was taken on 5 July 2020, in Berkeley, California (37.91°N, 122.28°W). The solid and dashed curves are experimental data and simulation results based on a local weather database (*37*), respectively. Measurements starting from 14:00 LDT were performed with the direct solar radiation blocked. Temperature observed after sunset show clear signs of the TARC shutting off thermal radiative cooling as its surface ambient temperature falls below T_{MIT}. (**B**) Measured ambient cooling power of TARC and white roof coating with direct solar radiation blocked in the outdoor environment. (**C**) T_s and the corresponding ε_w mapping of TARC over 24 hours and the full year for Berkeley. Also shown are the SCSES of TARC compared with all other materials with fixed solar absorptance (A_{ref}) and fixed thermal emittance (ε_{ref}). The icons in the SCSES map correspond to those used in Fig. 1C, denoting the radiative parameters (A, ε_w) of the strongest rival to TARC in source energy savings for the local climate (*36*).

membranes, we estimated the multilayered metamaterial to achieve comparable modulation performance ($\Delta\varepsilon_w > 0.8$) as the TARC we presented and would be producible in a roll-to-roll fashion (figs. S10 and S11). Roll-to-roll manufacturing of PE-based TARC would be beneficial because of its high scalability, low cost (*9*), and the fact that it is free from the liquid evaporation process in fabrication (*39*). The PE layer can be also replaced by other organic or inorganic materials with negligible optical loss in the wavelength ranges of both solar irradiation and IR atmospheric transparency window, so that the TARC technology can be designed specifically

to be endurable in different environmental conditions.

We developed a mechanically flexible, energy-free TARC for intelligent regulation of household temperature. Our system features a thermally driven metal-insulator transition in cooperation with photonic resonance, and demonstrates self-switching in sky-window thermal emittance from 0.20 to 0.90 at a desired temperature of ~22°C. These attractive properties enable switching of the system from the radiative cooling mode at high temperatures to the solar-heating or keep-warm mode at low temperatures in an outdoor setting. For most cities in the United States, our simulations indicate the TARC may outperform all conventional roof materials in terms of cutting energy consumption for households.

REFERENCES AND NOTES

1. US Energy Information Administration, "Annual Energy Review 2020" (2020); https://www.eia.gov/totalenergy/data/annual/
2. US Energy Information Administration, "2015 Residential Energy Consumption Survey" (2015); https://www.eia.gov/consumption/residential/
3. A. R. Gentle, G. B. Smith, *Adv. Sci. (Weinh.)* **2**, 1500119 (2015).
4. M. Dong, N. Chen, X. Zhao, S. Fan, Z. Chen, *Opt. Express* **27**, 31587–31598 (2019).
5. B. Orel, M. K. Gunde, A. Krainer, *Sol. Energy* **50**, 477–482 (1993).
6. P. Berdahl, M. Martin, F. Sakkal, *Int. J. Heat Mass Transf.* **26**, 871–880 (1983).
7. N. N. Shi *et al*., *Science* **349**, 298–301 (2015).
8. J. Kou, Z. Jurado, Z. Chen, S. Fan, A. J. Minnich, *ACS Photonics* **4**, 626–630 (2017).
9. Y. Zhai *et al*., *Science* **355**, 1062–1066 (2017).
10. J. Mandal *et al*., *Science* **362**, 315–319 (2018).
11. T. Li *et al*., *Science* **364**, 760–763 (2019).
12. Z. Li, Q. Chen, Y. Song, B. Zhu, J. Zhu, *Adv. Mater. Technol.* **5**, 1901007 (2020).
13. P. Berdahl, *Appl. Opt.* **23**, 370–372 (1984).
14. X. Li *et al*., *Cell Rep. Phys. Sci.* **1**, 100221 (2020).
15. G. Ulpiani, G. Ranzi, K. W. Shah, J. Feng, M. Santamouris, *Sol. Energy* **209**, 278–301 (2020).
16. K. Goncharov *et al*., "1500 W deployable radiator with loop heat pipe" (SAE Technical Paper 2001-01-2194, 2001); https://doi.org/10.4271/2001-01-2194.
17. C. Lashley, S. Krein, P. Barcomb, "Deployable radiators-A multi-discipline approach" (SAE Technical Paper 981691, 1998); https://doi.org/10.4271/981691.
18. H. Zhao, Q. Sun, J. Zhou, X. Deng, J. Cui, *Adv. Mater.* **32**, e2000870 (2020).
19. Z. Xia, Z. Fang, Z. Zhang, K. Shi, Z. Meng, *ACS Appl. Mater. Interfaces* **12**, 27241–27248 (2020).
20. H. Nagano, Y. Nagasaka, A. Ohnishi, *J. Thermophys. Heat Trans.* **20**, 856–864 (2006).
21. M. Ono, K. Chen, W. Li, S. Fan, *Opt. Express* **26**, A777–A787 (2018).
22. M. Chen, A. M. Morsy, M. L. Povinelli, *Opt. Express* **27**, 21787–21793 (2019).
23. S. Taylor, Y. Yang, L. Wang, *J. Quant. Spectrosc. Radiat. Transf.* **197**, 76–83 (2017).
24. W.-W. Zhang, H. Qi, A.-T. Sun, Y.-T. Ren, J.-W. Shi, *Opt. Express* **28**, 20609–20623 (2020).
25. K. Ito, T. Watari, K. Nishikawa, H. Yoshimoto, H. Iizuka, *APL Photonics* **3**, 086101 (2018).
26. K. Nishikawa, K. Yatsugi, Y. Kishida, K. Ito, *Appl. Phys. Lett.* **114**, 211104 (2019).
27. H. Kim *et al*., *Sci. Rep.* **9**, 11329 (2019).
28. K. Sun *et al*., *ACS Photonics* **5**, 2280–2286 (2018).
29. X. Xue *et al*., *Adv. Mater.* **32**, e1906751 (2020).
30. F. J. Morin, *Phys. Rev. Lett.* **3**, 34–36 (1959).
31. T.-L. Wu, L. Whittaker, S. Banerjee, G. Sambandamurthy, *Phys. Rev. B Condens. Matter Mater. Phys.* **83**, 073101 (2011).
32. C. Kim, J. S. Shin, H. Ozaki, *J. Phys. Condens. Matter* **19**, 096007 (2007).
33. S. Lee *et al*., *Science* **355**, 371–374 (2017).
34. A. S. Barker, H. W. Verleur, H. J. Guggenheim, *Phys. Rev. Lett.* **17**, 1286–1289 (1966).
35. J. Agassi, *Science* **156**, 30–37 (1967).
36. The materials and methods are available as supplementary materials.
37. US Department of Energy, "EnergyPlus Weather Data" (2021); https://energyplus.net/weather.
38. P. J. Rosado, R. Levinson, *Energy Build.* **199**, 588–607 (2019).
39. A. Leroy *et al*., *Sci. Adv.* **5**, eaat9480 (2019).

ACKNOWLEDGMENTS

Funding: This work was funded by the Office of Science, Office of Basic Energy Sciences, Materials Sciences and Engineering Division, US Department of Energy, under contract no. DE-AC02-05-CH11231 (EMAT program KC1201). Work at the Molecular Foundry was supported by the Office of Science, Office of Basic Energy Sciences, US Department of Energy, under contract no. DE-AC02-05CH11231. J.W. acknowledges support from a Bakar Prize. R.L. acknowledges support from the Assistant Secretary for Energy Efficiency and Renewable Energy, Building Technologies Office, of the US Department of Energy under contract no. DE-AC02-05CH11231. J.Y. acknowledges support from the National Science Foundation under grant no. 1555336. M.P.G. gratefully acknowledges the National Science Foundation for fellowship support under the National Science Foundation Graduate Research Fellowship Program. **Author contributions:** K.T., K.D. J.L., and J.W. conceived the general idea. K.T. and K.D. designed the device. K.T. fabricated the device. K.T., M.P.G., H.K., Q.W., A.J., J.J.U., and J.Y. contributed to the spectral characterizations. K.T., K.D., J.L. Y.R., and C.P.G. contributed to the solar simulator characterizations. K.T., J.L., and C.-Y.L. performed the vacuum chamber characterizations. K.T., K.D., J.L., and J.W. performed the field experiments. K.D., J.L. and J.Y. performed the numerical electromagnetic simulations. K.T., F.G.R., and R.L. performed all other simulations. All authors discussed and analyzed the results. K.T., K.D., J.L., and J.W. wrote the manuscript with assistance from other authors. All authors reviewed and revised the manuscript. **Competing interests:** R.L. is an unpaid, nonvoting member of the board of directors of the Cool Roof Rating Council (CRRC) and a paid consultant to the CRRC. K.T., K.D., J.L., and J.W. are inventors of a provisional patent application related to this work. The authors declare that they have no competing interests. **Data and materials availability:** All data required to evaluate the conclusions in the manuscript are available in the main text or the supplementary materials.

SUPPLEMENTARY MATERIALS

science.org/doi/10.1126/science.abf7136
Nomenclature
Materials and Methods
Supplementary Text
Figs. S1 to S19
Tables S1 to S6
References (*40*–*105*)

13 November 2020; resubmitted 5 May 2021
Accepted 26 October 2021
10.1126/science.abf7136

Science

Temperature-adaptive radiative coating for all-season household thermal regulation

Kechao TangKaichen DongJiachen LiMadeleine P. GordonFinnegan G. ReichertzHyungjin KimYoonsoo RhoQingjun WangChang-Yu LinCostas P. GrigoropoulosAli JaveyJeffrey J. UrbanJie YaoRonnen LevinsonJunqiao Wu

Science, 374 (6574), • DOI: 10.1126/science.abf7136

A passive turnoff

Passive radiative cooling technology uses the infrared atmospheric window to allow outer space to be a cold sink for heat. However, this effect is one that is only helpful for energy savings in the warmer months. Wang *et al*. and Tang *et al*. used the metal-insulator transition in tungsten-doped vanadium dioxide to create window glass and a rooftop coating that circumvents this problem by turning off the radiative cooling at lower temperatures. Because the transition is simply temperature dependent, this effect also happens passively. Model simulations suggest that these materials would lead to energy savings year-round across most of the climate zones in the United States. —BG

Science
AAAS

Supplementary Materials for

Temperature-adaptive radiative coating for all-season household thermal regulation

Kechao Tang *et al.*

Corresponding author: Junqiao Wu, wuj@berkeley.edu

Science **374**, 1504 (2021)
DOI: 10.1126/science.abf7136

The PDF file includes:

Nomenclature

Abbreviations

Ag	silver
BaF_2	barium fluoride
DI	deionized
FTIR	Fourier transform infrared
HF	hydrofluoric acid
HNO_3	nitride acid
HVAC	heating, ventilation, and air conditioning
IR	infrared
LDT	local daylight time
MIT	metal-insulator transition
N_2	nitrogen
NIR	near-infrared
O_2	oxygen
PE	polyethylene
PLD	pulsed laser deposition
SCSES	space conditioning source energy saving
Si	silicon
SF_6	sulfur hexafluoride
TARC	temperature-adaptive radiative coating
TIR	thermal infrared
TMY3	typical meteorological year 3
U.S.	United States
UV	ultraviolet
VO_2	vanadium dioxide
V_2O_5	vanadium pentoxide
WO_3	tungsten trioxide
$W_xV_{1-x}O_2$	tungsten-doped vanadium oxide
XeF_2	xenon difluoride

English Symbols

A	solar absorptance
A_{ref}	solar absorptance of reference materials
$B(\lambda, T)$	spectral radiance emitted by a black body at absolute temperature T
C	annual source energy uses for air conditioning
CF	cloud coverage factor
D_{c}	cooling degrees
D_{h}	heating degrees
ΔD_{c}	reduction in cooling degrees
ΔD_{h}	reduction in heating degrees
$\Delta D_{\mathrm{c,TARC}}$	reduction in cooling degrees by TARC
$\Delta D_{\mathrm{h,TARC}}$	reduction in heating degrees by TARC
F	annual fan source energy use
F_{c}	annual cooling fan source energy use
F_{h}	annual heating fan source energy use
H	annual source energy uses for gas heating
I	solar irradiance
$I_{\mathrm{s}}(\lambda)$	solar spectral irradiance
P_{Al}	measured heater power for Al surface in vacuum
P_{TARC}	measured heater power for TARC surface in vacuum
P''_{cool}	cooling flux (power/area) of TARC in vacuum
$P''_{\mathrm{cool\_amb}}$	cooling flux (power/area) of TARC in ambient
q_{c}	convective heat loss
q_{LW}	long-wave thermal radiative loss
q_{SW}	short-wave solar absorption
R	solar reflectance
$r(\lambda)$	spectral reflectance
T_{MIT}	metal-insulator-transition temperature
T_{a}	air temperature

T_{d}	dew point temperature
T_{s}	surface temperature
$T_{\mathrm{set,\ cool}}$	setpoint temperature for cooling
$T_{\mathrm{set,\ heat}}$	setpoint temperature for heating
ΔS	annual space-conditioning source energy savings
ΔS_{c}	annual space cooling source energy savings
ΔS_{h}	annual space heating source energy savings
S_{TARC}	space-conditioning source energy consumption of TARC
v	wind speed

Greek Symbols

α_{c}	linear fitting coefficient relating ΔS_{c} to ΔD_{c}
α_{h}	linear fitting coefficient relating ΔS_{h} to ΔD_{h}
$a(\lambda)$	spectral absorptance
$\mathcal{A}$	surface area
β_{c}	linear-fit coefficient relating F_{c} to C
β_{h}	linear-fit coefficient relating F_{h} to H
γ	calibration factor for thermal emittance between vacuum and ambient conditions
$\varepsilon_{\mathrm{ref}}$	sky-window thermal emittance of reference materials
ε_{w}	sky-window thermal emittance
$\varepsilon_{\mathrm{vac}}$	thermal emittance in vacuum
$\varepsilon_{\mathrm{clear\_sky}}$	sky emissivity in a clear-sky model
$\varepsilon_{\mathrm{sky}}$	sky emissivity with cloud correction
$\varepsilon(\lambda)$	spectral emittance

Materials and Methods

Preparation of the TARC

675 μm-thick Si wafers were first covered with an approximately 2 μm thick polyimide film (PI-2545, HD MicroSystems LLC) via spin coating, which was then cured in a N_2-filled oven at 425 °C for 60 minutes. The polyimide film acts as an etching protection layer for the final transfer process. $W_xV_{1-x}O_2$ thin films were grown on the polyimide layer using pulse laser deposition (PLD). The PLD target was prepared by mixing WO_3 and V_2O_5 powders with a W:V atomic ratio at 1.5%, then made into 2.5 cm diameter round discs with a hydraulic press. All $W_xV_{1-x}O_2$ thin films were deposited in a 5 mTorr O_2 environment at 500 °C substrate temperature, and the PLD laser energy was set at 321 mJ with 10 Hz pulse frequency. 70 nm of $W_xV_{1-x}O_2$ was grown at a rate of 6 nm/min, followed by a post-deposition anneal at 500 °C for 30 mins in the same 5 mTorr O_2 environment. The metamaterials patterns were made with standard photolithography, combined with etching of $W_xV_{1-x}O_2$ by SF_6 + O_2 in a plasma etching system. After removing the photoresist with acetone and O_2 plasma, 1.5 μm thick BaF_2 and 100 nm thick Ag layers were grown sequentially on top via thermal evaporation. The growth rates of BaF_2 and Ag were controlled at 20 Å/s and 2 Å/s, respectively.

In the transfer process, a piece of 0.06 mm thick single-sided sticky cellophane packaging tape was first carefully applied to fully cover the surface, where the Ag layer was stuck to the adhesive side without any residual air bubbles. An initial Si substrate removal process was performed in a HF + HNO_3 solution, mixed by aqueous HF (49% weight percentage) and HNO_3 solution (68% weight percentage) with a volume ratio of 10:1. The samples were taken out and rinsed with DI water to stop the initial etching when the etchant starts to touch down on the polyimide layer. A XeF_2 dry etching process was then carried out to clean off the residue Si. In the final step, the polyimide protection layer was removed by O_2 plasma at 100 mTorr O_2 pressure and 200 W plasma power for about 11 mins.

Spectrally resolved measurements

Thermal spectral reflectance at normal incidence, $r(\lambda,T)$, was characterized by a Nicolet iS50 FTIR spectrometer and Nicolet Continuum microscope over the spectrum 5-15 μm. The objective lens was 32× with 0.65 numerical aperture. A blade aperture of 100 μm × 100 μm was used to select the area of interest. All reflection spectra were normalized to the reflection spectrum of a 300 nm thick gold film. The temperature of the samples (15-50 °C) was controlled by a customized closed-loop thermal stage, connected to a Lakeshore 321 temperature controller. Kirchhoff's law of radiation states that in thermodynamic equilibrium, spectral emittance $\varepsilon(\lambda,T)$ equals spectral absorptance $a(\lambda,T)$. Since the TARC was essentially opaque from 5 to 15 μm, its thermal spectral emittance in this range was computed as $\varepsilon(\lambda,T) = a(\lambda,T) = 1 - r(\lambda,T)$. Near normal-hemispherical solar spectral reflectance, $r(\lambda)$, was measured from 300 to 2,500 nm with an Agilent Cary 5000 UV-vis-NIR spectrometer equipped with an Internal Diffuse Reflectance Accessory (DRA-2500), which collects both specular and diffuse reflections. Solar spectral absorptance was computed as $a(\lambda) = 1 - r(\lambda)$ since the film was essentially opaque to sunlight.

The solar absorptance A and sky-window thermal emittance ε_s can be calculated from the corresponding spectral data by:

$$A = \left(\int_{0.3\ \mu m}^{2.5\ \mu m} I_s(\lambda)\, a(\lambda)\, d\lambda\right) / \left(\int_{0.3\ \mu m}^{2.5\ \mu m} I_s(\lambda)\, d\lambda\right)$$

$$\varepsilon_w(T) = \left(\int_{8\ \mu m}^{13\ \mu m} B(\lambda)\, \varepsilon(\lambda,T)\, d\lambda\right) / \left(\int_{8\ \mu m}^{13\ \mu m} B(\lambda)\, d\lambda\right)$$

where $I_s(\lambda)$ is the solar spectral irradiance, and $B(\lambda)$ is the spectral radiance of a black body emission.

Thermal infrared imaging and analysis

TIR images were captured by a FLIR ONE infrared (IR) camera working at a wavelength range of 8-13 μm (same as the sky window). To minimize the reflection from the camera and the surroundings, the default viewing angle was set as 15° instead of normal incident direction, and the experiments were performed in an open-area, outdoor environment under a clear (cloud-free) sky. When taking TIR images, the camera measures the incident TIR radiation, and then gives the temperature reading (T_{TIR}) assuming a constant thermal emittance for the target (e.g., 0.90, the default setting of the camera).

Simulation of device properties

The spectral absorptance of TARC is numerically calculated using COMSOL Multiphysics, with all the geometric parameters matching the original design. Material properties in IR and visible ranges are from Refs. (*40-43*) and (*44-46*), respectively. Note that to better predict the actual TARC performance in the 5-15 μm range, the imaginary part of BaF_2 permittivity is slightly increased by $\Delta\varepsilon_i = 0.022\lambda - 0.049$ (unit of λ is μm) by fitting.

Characterization of thermal emittance modulation in vacuum condition

In the measurement setup shown in Fig. 3A, the power of the heater at the equilibrium surface temperature *T* for the Al foil surface is denoted as $P_{\mathrm{Al}}(T)$, and the power for the TARC surface is denoted as $P_{\mathrm{TARC}}(T)$. $P_{\mathrm{Al}}(T)$ and $P_{\mathrm{TARC}}(T)$ are:

$$P_{\mathrm{Al}}(T) = \sigma\,\mathcal{A}\,\varepsilon_{\mathrm{Al}}\,(T^4 - T_{\mathrm{env}}^4) + C(T)$$

$$P_{\mathrm{TARC}}(T) = \sigma\,\mathcal{A}\,\varepsilon_{\mathrm{TARC,v}}\,(T^4 - T_{\mathrm{env}}^4) + C(T)$$

Here σ is the Stefan-Boltzmann constant, $\mathcal{A}$ is the area of the sample surface, $\varepsilon_{\mathrm{Al}}$ and $\varepsilon_{\mathrm{TARC,v}}$ are effective thermal emittance of Al and TARC in vacuum conditions, T_{env} is the temperature of the environment (chamber wall), $C(T)$ represents ancillary heat loss power from other radiative source and thermal conduction, and all temperatures are absolute. The ancillary loss is temperature dependent and unknown, but is reasonably assumed to be the same for the surface conditions of the two materials. The inner walls of the vacuum chamber can be treated as a black body due to two reasons: (1) High-emittance tape was used to cover the inner walls (see Fig. S12); (2) The sample area (16 cm^2) is much smaller than the total area of the inner walls (1,500 cm^2) (*47*). Therefore, the cooling flux (power/area) contributed by the TARC, denoted as $P''_{\mathrm{cool}}(T)$, can be calculated as:

$$P''_{\mathrm{cool}}(T) = [P_{\mathrm{TARC}}(T) - P_{\mathrm{Al}}(T)]/\mathcal{A} = \sigma\,(\varepsilon_{\mathrm{TARC,v}} - \varepsilon_{\mathrm{Al}})\,(T^4 - T_{\mathrm{env}}^4)$$

In this equation, σ is known, $\varepsilon_{\mathrm{Al}}$ is approximated as 0.03, and T_{env} is equal to the temperature of the cryogen (195 K, or -78 °C). Therefore, $\varepsilon_{\mathrm{TARC,v}}$ at the I state and the M state can be obtained by fitting $P''_{\mathrm{cool}}(T)$ with *T* at two branches before and after MIT. The error bars in Fig. 3B come from the uncertainty of $\varepsilon_{\mathrm{Al}}$ (taken as 0.02) and a systematic error ϵ_{s} (taken as 8.0 W/m^2) in the measurement of $P''_{\mathrm{cool}}(T)$ arising from the limitation of the tool and the power instability. We note that the fitted $\varepsilon_{\mathrm{TARC,v}}$ is the thermal emittance in the vacuum condition, and can be related to the ambient condition thermal emittance $\varepsilon_{\mathrm{TARC,w}}$ by

$$\varepsilon_{\mathrm{TARC,v}} = \gamma \cdot \varepsilon_{\mathrm{TARC,w}}$$

in which the coefficient γ is calculated to be about 0.7 from the spectra of TARC (Fig. S4), and is coincidentally the same for both the M state and the I state.

Simulation of surface temperature

The stabilized temperature of a surface (T_{s}) with given solar absorptance (*A*) and thermal emittance (ε) was calculated based on adiabatic approximation, assuming negligible heat transfer between the

surface and the underlying structure. The key climate parameters for a specific city or region, including air temperature (T_a), dew point temperature (T_d), wind speed (v), solar irradiance (I) and cloud coverage factor (CF) are obtained from TMY3 weather files available from the U.S. Department of Energy (*37*). The thermal emittance of the TARC was set at 0.20 for T_s < 19 °C and 0.90 for T_s > 27 °C, and approximated by a linear interpolation in the transition region (19 °C $\leqslant$ $T_s \leqslant$ 27 °C). Based on this setup, the all-year-around temperature map (Fig. 4C) of TARC and of all conventional materials with an arbitrary combination of static A and ε were calculated and compared. More details of the simulation can be found in the Supplementary Text, Note A, Section I.

Projection of energy savings

In hour-of-year i, we define heating degrees $D_{\mathrm{h},i} = \left(T_{\mathrm{set,heat}} - T_{\mathrm{s},i}\right)_+$ and cooling degrees $D_{\mathrm{c},i} = \left(T_{\mathrm{s},i} - T_{\mathrm{set,cool}}\right)_+$, where $x_+ = x$ if $x > 0$, or 0 otherwise. The annually averaged heating degrees and cooling degrees are denoted by D_{h} and D_{c}, respectively.

Rosado & Levinson (*38*) simulated the annual space heating source energy savings ΔS_{h} (typically negative) and the annual space cooling source energy savings ΔS_{c} (typically positive) attained by increasing roof albedo for various categories and vintages of buildings in 15 U.S. climates zones and 16 California climate zones. All savings are normalized to roof area. Note that ΔS_{h} and ΔS_{c} are not directly presented by Rosado & Levinson but can be estimated from the heating, cooling, and fan energy uses reported in that work, as described in Appendix I of the Supplementary Text.

Summing ΔS_{h} and ΔS_{c} yields the annual space-conditioning (heating + cooling) source energy savings ΔS. U.S. cool-roof space heating energy savings ΔS_{h} and space cooling energy savings ΔS_{c} reported by Rosado & Levinson are regressed against our own calculations of the reductions in annual average heating degrees ΔD_{h} and cooling degrees ΔD_{c}, respectively. These linear fits of the form $\Delta S_{\mathrm{h}} = \alpha_{\mathrm{h}}\,\Delta D_{\mathrm{h}}$ and $\Delta S_{\mathrm{c}} = \alpha_{\mathrm{c}}\,\Delta D_{\mathrm{c}}$ yield $\Delta S = \alpha_{\mathrm{h}}\,\Delta D_{\mathrm{h}} + \alpha_{\mathrm{c}}\,\Delta D_{\mathrm{c}}$. Specifically, energy simulations for four static roofing materials with ε_{w} = 0.90 and solar reflectance R = 0.10, 0.25, 0.40, or 0.60 ($A = 1 - R$ = 0.90, 0.75, 0.60, or 0.40) were selected for the extraction of the coefficients α_{h} and α_{c} using the material with A = 0.90 as the baseline.

To evaluate the potential space-conditioning source energy savings (SCSES) per unit roof area obtained by using TARC instead of a reference roofing surface with static solar absorptance A_{ref} and static thermal emittance $\varepsilon_{\mathrm{ref}}$, we calculated, in each city, $\Delta D_{\mathrm{h,TARC}}(A_{\mathrm{ref}}, \varepsilon_{\mathrm{ref}}) \equiv D_{\mathrm{h,TARC}} - D_{\mathrm{h}}(A_{\mathrm{ref}}, \varepsilon_{\mathrm{ref}})$ and $\Delta D_{\mathrm{c,TARC}}(A_{\mathrm{ref}}, \varepsilon_{\mathrm{ref}}) \equiv D_{\mathrm{c,TARC}} - D_{\mathrm{c}}(A_{\mathrm{ref}}, \varepsilon_{\mathrm{ref}})$, varying A_{ref} and $\varepsilon_{\mathrm{ref}}$ from 0 to 1. We then computed space-conditioning source energy savings $\Delta S_{\mathrm{TARC}}(A_{\mathrm{ref}}, \varepsilon_{\mathrm{ref}}) = \alpha_{\mathrm{h}}\,\Delta D_{\mathrm{h,TARC}}(A_{\mathrm{ref}}, \varepsilon_{\mathrm{ref}}) + \alpha_{\mathrm{c}}\,\Delta D_{\mathrm{c,TARC}}(A_{\mathrm{ref}}, \varepsilon_{\mathrm{ref}})$ for each building category and vintage of interest. The minimum $\Delta S_{\mathrm{TARC}}(A_{\mathrm{ref}}, \varepsilon_{\mathrm{ref}})$ (namely, $\mathrm{SCSES_{min}}$) for all possible existing roof coating properties is taken as the figure of merit for each combination of local climate, building category, and vintage group. In Fig. 1C and Fig. 4C, we used three different icons to represent three different types of competing materials where $\mathrm{SCSES_{min}}$ occurs --- that is, the strongest rivals to TARC in energy saving. The triangle, circle, and square icons represent metallic, white, and dark roof coatings, with typical (A_{ref}, $\varepsilon_{\mathrm{ref}}$) parameters around (0.35, 0.25), (0.05, 0.95), and (0.95, 0.95), respectively.

The results in both Fig. 1C and Fig. 4C are based on the dominant resident building prototype in the U.S. (*48*), which is a single-family home built prior to 1980. Minimum annual source energy savings per unit roof area for single-family homes and apartment buildings built before 1980, between 1980 and 1999, and recently are presented in Table S4.

Supplementary Text

Note A. Simulations of surface temperature and energy saving advantage of TARC

Section I. Calculation of surface temperature in adiabatic approximation

The stabilized surface temperature of TARC and any material with given solar absorptance (*A*) and sky-window thermal emittance (ε_{w}) can be calculated based on the adiabatic approximation (*49*), assuming negligible heat exchange with the underlying structure. The thermal equilibrium is balanced by the three heat exchange components on the surface, which are net long-wave thermal radiative loss (q_{LW}), short-wave solar absorption (q_{SW}), and convective heat loss (q_{c}), respectively. The equation for thermal equilibrium is denoted as

$$q_{\mathrm{SW}} - q_{\mathrm{LW}} - q_{\mathrm{c}} = 0 \tag{S1}$$

Each term can be expanded as

$$q_{\mathrm{SW}} = A \cdot I \tag{S2}$$

$$q_{\mathrm{LW}} = \varepsilon_{\mathrm{w}}(T_{\mathrm{s}}) \cdot \sigma\left(T_{\mathrm{s}}^4 - T_{\mathrm{sky}}^4\right) \tag{S3}$$

$$q_{\mathrm{c}} = h_{\mathrm{c}}(T_{\mathrm{s}} - T_{\mathrm{a}}) \tag{S4}$$

In these equations, I is the solar irradiance, T_{s} is the absolute surface temperature, T_{sky} is the absolute sky temperature, h_{c} is the convective heat transfer coefficient, and T_{a} is the absolute air temperature. The model schematic is shown in Fig. S16. We note that though Eq. (S3) is typically applied to broad-band IR emitters with uniform spectral emittance from 2 μm to 30 μm, it can be safely extended to the case of TARC. To support this argument, we calculated the net radiative cooling power for TARC and that of a broad-band emitter with constant emittance equal to ε_{w} of TARC. The general form of net radiative cooling power P_{net} is:

$$P_{\mathrm{net}} = P_{\mathrm{rad}} - P_{\mathrm{atm}} \tag{S5}$$

$$P_{\mathrm{rad}} = \iint B(\lambda, T_{\mathrm{s}})\varepsilon_{\mathrm{s}}(\lambda, \Omega, T_{\mathrm{s}})\cos\theta d\Omega d\lambda \tag{S6}$$

$$P_{\mathrm{atm}} = \iint B(\lambda, T_{\mathrm{a}})\varepsilon_{\mathrm{atm}}(\lambda, \Omega)\varepsilon_{\mathrm{s}}(\lambda, \Omega, T_{\mathrm{s}})\cos\theta d\Omega d\lambda \tag{S7}$$

in which P_{rad} and P_{atm} are radiative power of the surface and absorbed radiation power from the atmosphere, respectively; B is the black body spectral radiance; ε_s is the surface's spectral emittance; and $\varepsilon_{\mathrm{atm}}$ is the atmospheric spectral emittance. For simplicity, we assume that TARC is in M state when $T_{\mathrm{s}} \geq 25$ °C, and in I state when $T_{\mathrm{s}} \leq 20$ °C. The ε_s of the M state and the I state can be found in Fig. S4, and $\varepsilon_{\mathrm{atm}}$ is retrieved from previous studies (*50*). The spectral integration range is 2-30 μm. The results are presented in Fig. S17, showing that the net radiative cooling power of TARC and the broad-band emitter are very similar for different scenarios, with deviation < 10% even for extreme conditions ($T_{\mathrm{s}} - T_{\mathrm{a}} > 20$ °C). Therefore, the approximation of TARC as a broad-band emitter in the calculation of long-wave radiative power (q_{LW}) is valid.

The solar irradiance (I) and the air temperature (T_{a}) can be directly imported from the TMY3 weather files included in the EnergyPlus climate database (*37*). For an infinitely large surface, the convective heat transfer coefficient (h_{c}, W/(m^2·K)) is related to the wind speed (v, m/s) by (*51*)

$$h_{\mathrm{c}} = 5.6 + 5.1 \times \sqrt{v} \tag{S8}$$

The sky temperature is approximated by

$$T_{\mathrm{sky}}^4 = \varepsilon_{\mathrm{sky}} \cdot T_{\mathrm{a}}^4 \tag{S9}$$

$$\varepsilon_{\mathrm{sky}} = \varepsilon_{\mathrm{clear\_sky}} + 0.8(1 - \varepsilon_{\mathrm{clear\_sky}}) \cdot \mathrm{CF} \tag{S10}$$

$$\varepsilon_{\mathrm{clear\_sky}} = 0.754 + 0.0044 \times T_{\mathrm{d}} \tag{S11}$$

following a clear-sky model (*52*) combined with cloud correction (*53*), and the sky emissivity is denoted as $\varepsilon_{\mathrm{clear\_sky}}$ and $\varepsilon_{\mathrm{sky}}$ in each model, respectively. T_{d} is the dew point temperature (in °C) and CF is the cloud factor (ranging from 0 to 1; 0 for no clouds and 1 for full coverage), each of which is available in the climate database. The solar absorptance A and the thermal emittance ε are property parameters for the materials either pre-set (for reference materials) or obtained from experimental characterization (for TARC). Note that for TARC, $\varepsilon_{\mathrm{w}}(T_{\mathrm{s}})$ is set to 0.20 for T_{s} < 19 °C and to 0.90 for T_{s} > 27 °C, and approximated by a linear interpolation in the transition region (19 °C $\leqslant T_{\mathrm{s}} \leqslant$ 27 °C). The only unknown parameter T_s can thus be calculated by solving equations (S1-S4).

Fig. S18 shows an example of the simulated surface temperature mapping over the year for Baltimore, MD. The map is divided by 24 hour-period in one day and 12 months over one year. Each block shows the hour-of-day average temperature in a given month. Each hourly surface temperature can be calculated from the weather data in the corresponding time slot and the material parameters. The generation of T_{s} mapping over one year can be applied beyond TARC to other conventional materials with fixed A and ε. This method can also be extended to any other regions provided that the local climate information is available.

Section II. Energy saving advantage of TARC compared to conventional materials

The annual space heating source energy savings ΔS_{h} and annual space cooling source energy savings ΔS_{c} can be projected from the corresponding heating degrees reduction $\Delta D_{\mathrm{h,TARC}}(A_{\mathrm{ref}}, \varepsilon_{\mathrm{ref}})$ and cooling degrees reduction $\Delta D_{\mathrm{c,TARC}}(A_{\mathrm{ref}}, \varepsilon_{\mathrm{ref}})$, as described in the main text and the Materials and Methods section. The space conditioning source energy saving (SCSES) can be obtained by summing ΔS_{h} and ΔS_{c}, and an example of SCSES mapped with A_{ref} and $\varepsilon_{\mathrm{ref}}$ (each ranging from 0 to 1) for Baltimore is plotted in Fig. S19. The dashed boxes in the right panel of Fig. S19 correspond to the parameters of currently available roof coatings. The minimum point within the dashed box regions denotes the material that leads to the minimum space conditioning source energy saving ($\mathrm{SCSES_{min}}$) compared to all other roof coatings. In other words, for each city, the most energy-saving material (with fixed A_{ref} and $\varepsilon_{\mathrm{ref}}$) is first selected from all existing roof materials, and then compared with TARC. Thus, $\mathrm{SCSES_{min}}$ is the additional source energy saving of TARC compared to that "existing best energy-saving material". $\mathrm{SCSES_{min}}$ is taken as the figure of merit of TARC for the local climate and used to plot the mapping in Fig. 1C. In this example, the value for Baltimore is 22.4 MJ/(m^2·y), suggesting that would yield at least an annual source energy saving of 2.64 GJ over any other existing roof coating materials for a typical single-family building with a roof area of 118 m². Note that both the example in Fig. S18 and the map in Fig. 1C are based on the building prototype of single-family house built prior to 1980, which is the dominant residential building type in the U.S. according to the 2015 Residential Energy Consumption Survey microdata (*2*). The extracted coefficients for this and for other building prototypes can be found in Tables S2 and S3. The calculated $\mathrm{SCSES_{min}}$ for all residential building

prototypes (including those plotted in Fig. 1C) can be found in Table S4. The minimum coefficient of determination R^2 when fitting α_h and α_c for all cases is about 0.98.

Appendix I. Estimation of space-heating source energy saving (ΔS_h) and space cooling source energy saving (ΔS_c)

Rosado & Levinson (*38*) report for residential and commercial buildings across California and the United States gas heating (H), air conditioning (C), and fan (F) annual source energy uses in the heating, ventilation, and air conditioning (HVAC) system. Some of the fan energy is used to deliver heated air, and some is used to deliver cooled air. To calculate space heating source energy use S_h and space cooling source energy use S_c, we split annual fan source energy use into annual heating fan source energy use F_h and annual cooling source fan energy use F_c:

$$F = F_h + F_c \tag{S12}$$

The simplest scheme is to assume that F_h is proportional to H and that F_c is proportional to C:

$$F_h = \beta_h H \tag{S13}$$

$$F_c = \beta_c C \tag{S14}$$

We use subscript 1 to refer to the baseline condition, such that:

$$F_{h,1} = \beta_h H_1 \tag{S15}$$

$$F_{c,1} = \beta_c C_1 \tag{S16}$$

$$F_1 = F_{h,1} + F_{c,1} \tag{S17}$$

Since β_h and β_c are assumed to be constant for each building prototype (combination of building category, vintage, and location), we have similar expressions for gas heating source energy savings ΔH, air conditioning source energy savings ΔC, and fan source energy savings ΔF relative to the baseline:

$$\Delta F_h = \beta_h \Delta H \tag{S18}$$

$$\Delta F_c = \beta_c \Delta C \tag{S19}$$

$$\Delta F = \Delta F_h + \Delta F_c \tag{S20}$$

Combining Eqs. (S15) to (S20) yields:

$$\beta_h = \frac{F_1 \Delta C - C_1 \Delta F}{H_1 \Delta C - C_1 \Delta H} \tag{S21}$$

$$\beta_c = \frac{H_1 \Delta F - F_1 \Delta H}{H_1 \Delta C - C_1 \Delta H} \tag{S22}$$

The baseline refers to the condition where ε_w = 0.90 and A = 0.90, and the source energy uses are H_1, C_1, and F_1. The source energy savings ΔH, ΔC, and ΔF for conditions with other A values (0.75, 0.60, 0.40) are available in the savings database described in the Section 2.8 of Rosado & Levinson (*38*).

Finally, the space heating energy saving ΔS_h and space cooling energy saving ΔS_c can be calculated as:

$$\Delta S_{\mathrm{h}} = \Delta H + \Delta F_{\mathrm{h}} = (1 + \beta_{\mathrm{h}})\, \Delta H \tag{S23}$$

$$\Delta S_{\mathrm{c}} = \Delta C + \Delta F_{\mathrm{c}} = (1 + \beta_{\mathrm{c}})\, \Delta C \tag{S24}$$

Supplementary Figures

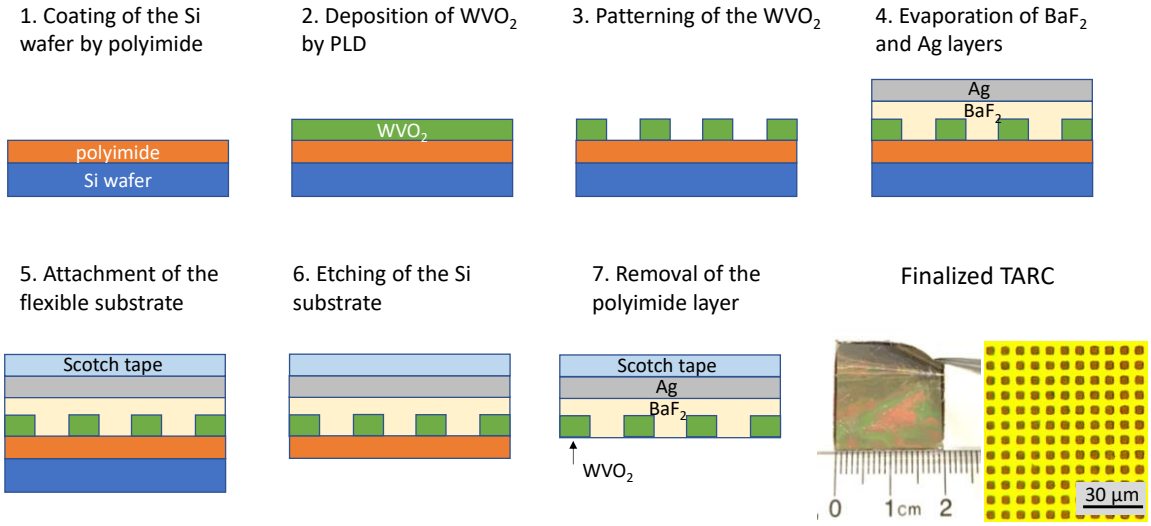

Figure S1. Schematics and pictures for the fabrication of TARC.

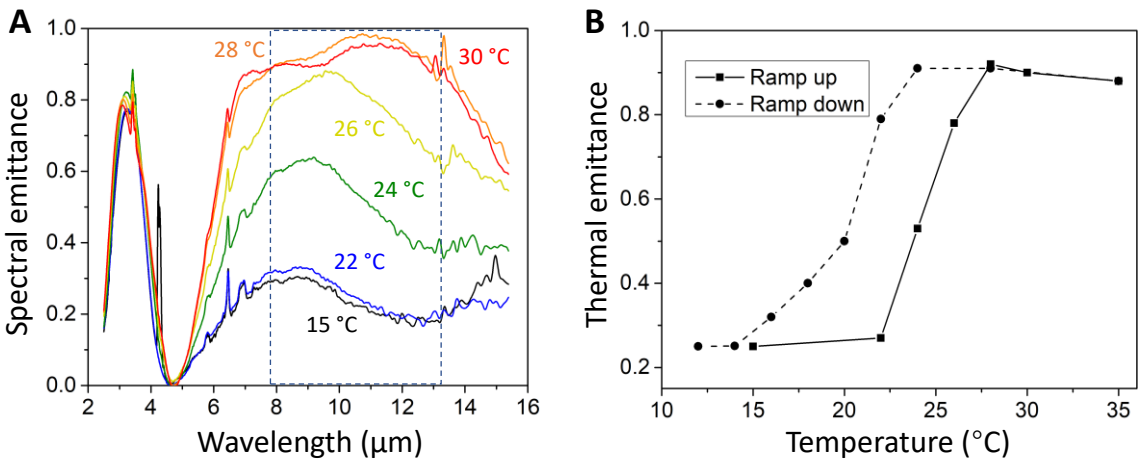

Figure S2. Detailed infrared spectra of TARC by Fourier transform infrared (FTIR) spectroscopy over the metal-insulator transition of $W_xV_{1-x}O_2$ (x=1.5%). A. Spectral emittance of TARC at temperatures ranging from 15 °C to 30 °C (ramp-up branch). The dashed box bounds the sky window (8-13 μm). **B.** Sky-window emittance as a function of TARC surface temperature, including both the ramp-up and ramp-down branches.

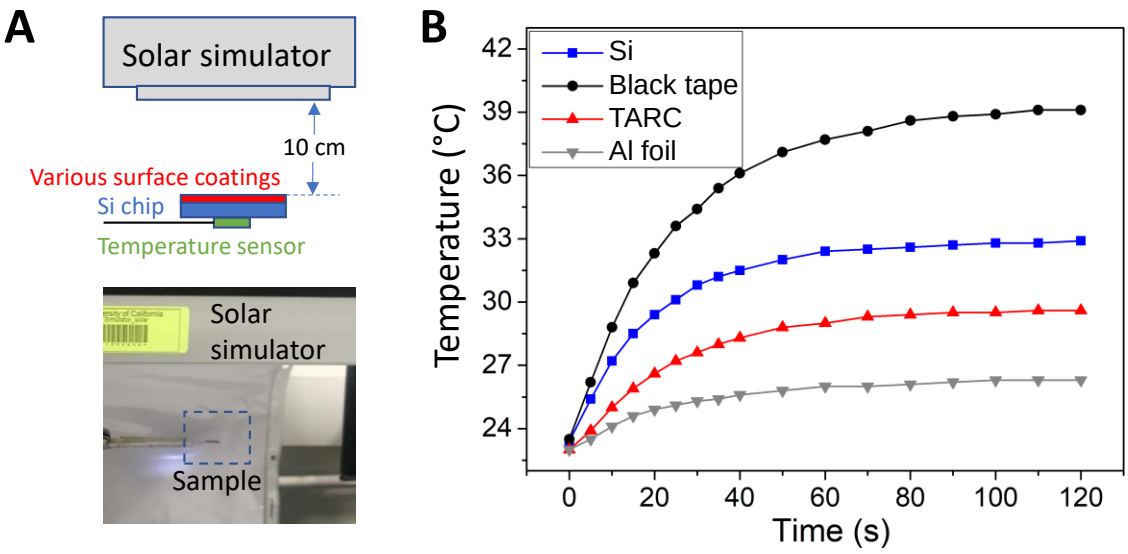

Figure S3. Global solar absorptance characterization of TARC. A. The schematic and a photo of the experiment setup. Various coatings were attached onto the top of a 1 cm × 1 cm Si chip, which was placed under a solar simulator (SS50B, Photo Emission Tech., Inc.). The temperatures were measured by a Pt temperature sensor. Before the measurement of each type of material surfaces, the shutter of the solar simulator remained closed, and the sample was first stabilized at the room temperature. Then the shutter was opened and the surface temperature was measured as a function of time. Only one sample was measured at one time, and this operation procedure was performed for four different surface coatings, maintaining the same setup geometry. The irradiance on the sample surface was 1 kW/m^2. **B.** Measured temperature as a function of exposure time for different top coatings. The time when the shutter was opened is defined to be 0 s. The stabilized temperature is linearly related to the absorbed heat power and thus solar absorptance A. Based on the solar absorptance of other references (A_{Si} = 0.50, A_{tape} = 0.95, A_{Al} = 0.10), A_{TARC} could be extracted as approximately 0.30, consistent with the theoretical prediction and other experimental results.

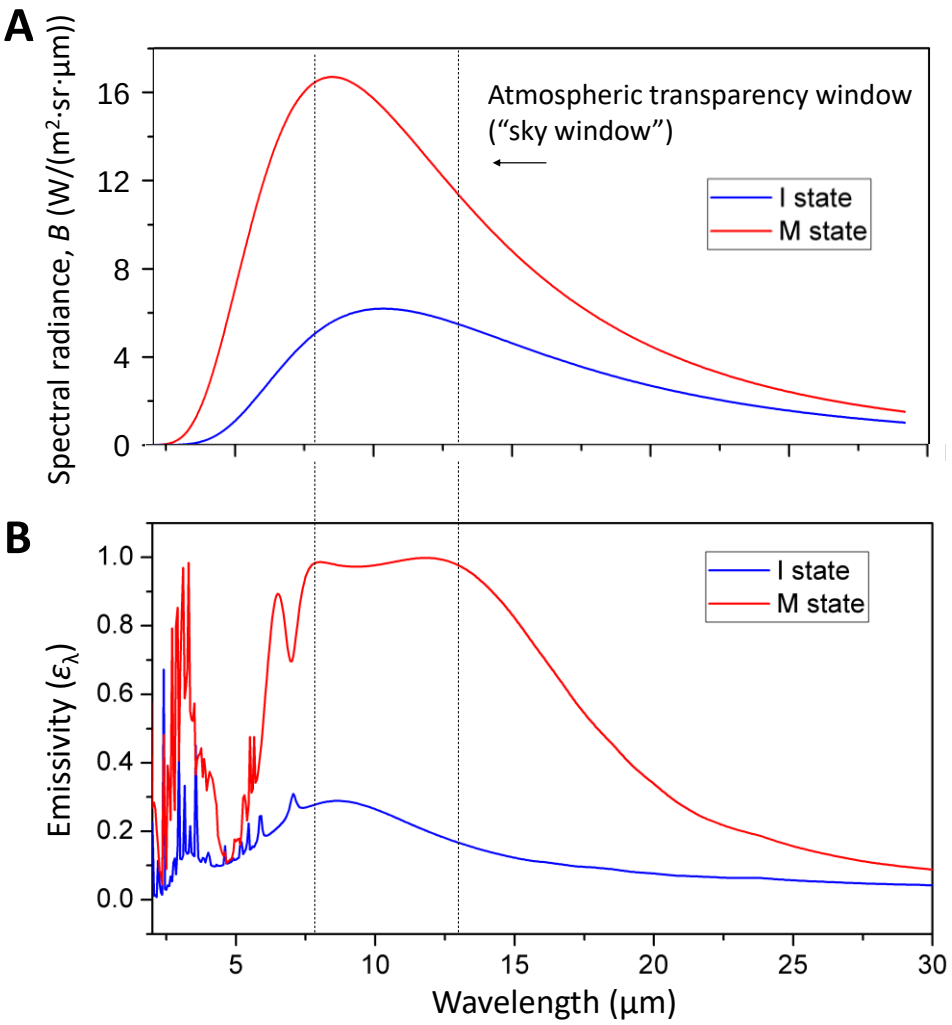

Figure S4. Calibration of thermal emittance. A. Spectral radiance of a blackbody at 0 °C and 60 °C. **B.** COMSOL-simulated spectral emittance of TARC in I state and in M state at wavelengths from 2 μm to 30 μm. The atmospheric transparency window is indicated by the grey dashed lines. Unlike the sky-window emittance, which is defined as $\varepsilon_w = \left(\int_{8\ \mu m}^{13\ \mu m} B(\lambda,T)\ \varepsilon(\lambda)\ d\lambda\right)/\left(\int_{8\ \mu m}^{13\ \mu m} B(\lambda,T)\ d\lambda\right)$, the effective thermal emittance in vacuum environment is denoted as $\varepsilon_{vac} = \left(\int_0^{\infty} B(\lambda,T)\ \varepsilon(\lambda)\ d\lambda\right)/\left(\int_0^{\infty} B(\lambda,T)\ d\lambda\right) \approx \left(\int_{2\ \mu m}^{30\ \mu m} B(\lambda,T)\ \varepsilon(\lambda)\ d\lambda\right)/\left(\int_0^{\infty} B(\lambda,T)\ d\lambda\right)$ (*28*), where $B(\lambda,T)$ is the spectral radiance of a blackbody. Based on the predicted spectral emittance of TARC, these two terms are related by $\varepsilon_{vac} = \gamma \cdot \varepsilon_w$, in which γ is about 0.7 for both the I state and the M state.

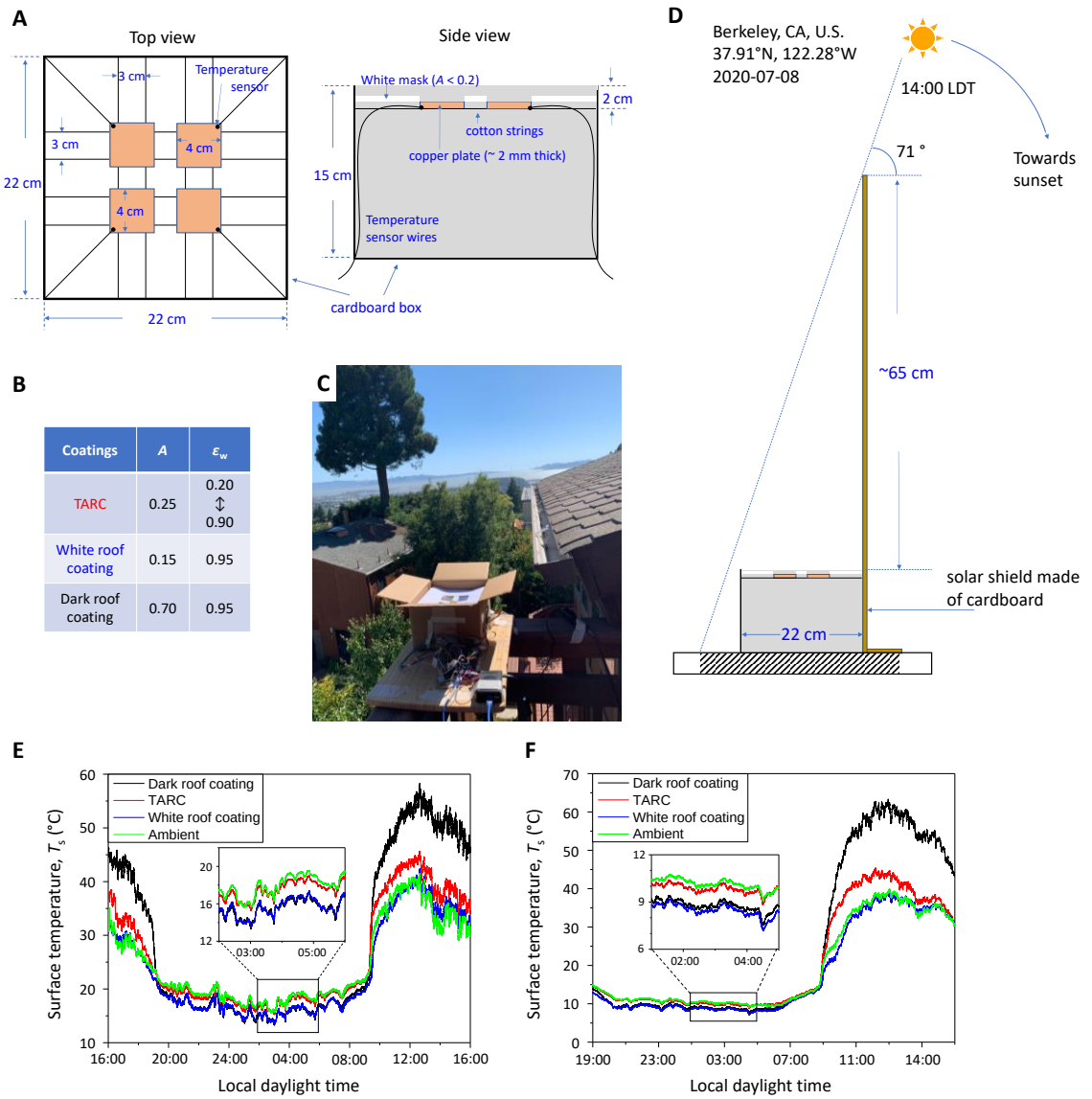

Figure S5. Details of the outdoor performance characterization of TARC. A. Schematic showing structure, geometry, and materials of the experimental setup. Identical 4 cm × 4 cm copper plates covered with different coatings were suspended by thin cotton strings (< 1 mm in diameter) in a cardboard box. A white paper mask was placed on top of the strings to minimize undesirable thermal artifacts from solar heating. **B.** Solar absorption and sky-window IR emittance of the measured material surfaces. **C.** A photo of the actual experiment setup. The measurement was carried out in an open-space rooftop balcony in Berkeley, CA (37.91°N, 122.28°W), with temperature time series recorded by a customized automatic temperature reading system. **D.** Schematic showing the solar shield used to block the direct solar radiation on the samples after 14:00 LDT. **E-F.** Additional experimental results measured on different days.

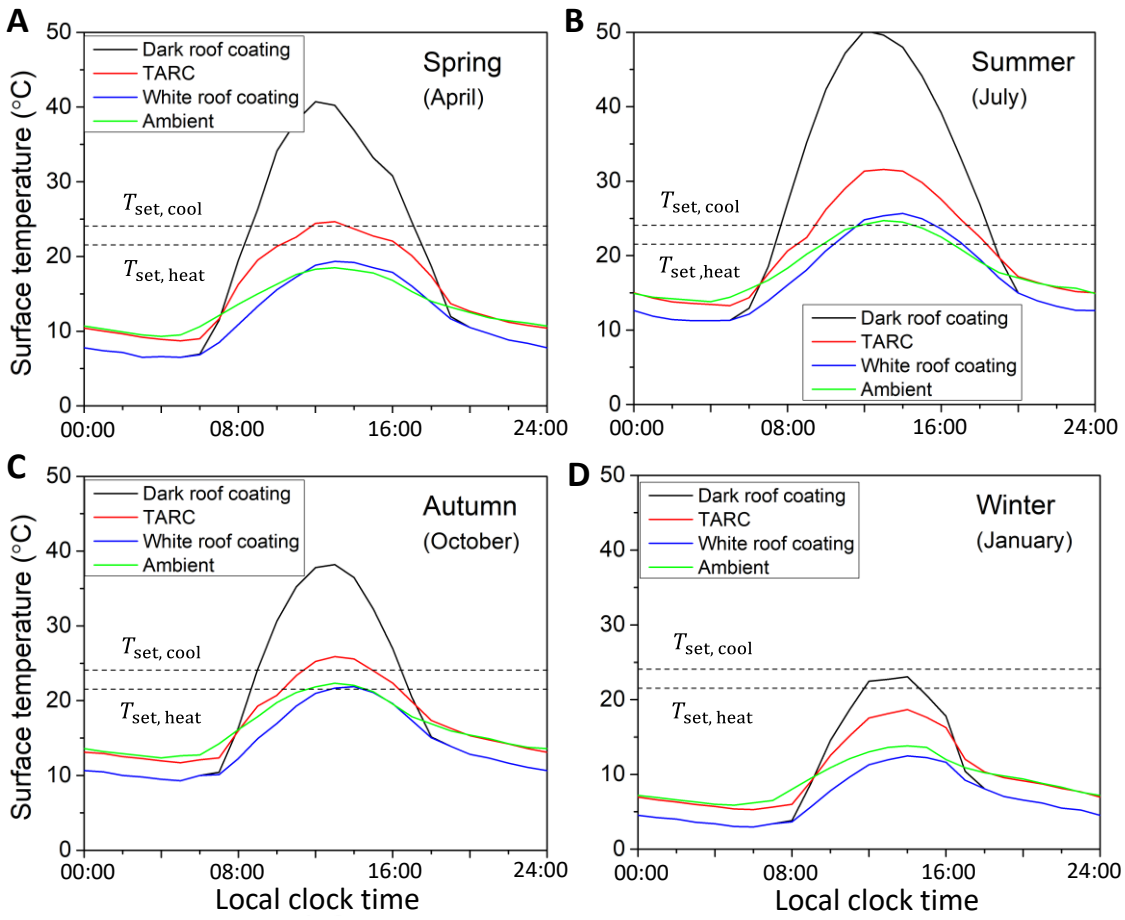

Figure S6. **Simulation of the surface temperature of a dark roof coating, TARC, and a white roof coating (the same three samples as those in Fig. 4) in four seasons in Berkeley, California (37.91°N, 122.28°W).** The ambient temperature data (green curves) are directly imported from the climate database (*37*) used for the simulation. The only condition where the white roof coating has an advantage over the TARC in energy saving is the daytime in summer (B), while for almost all other conditions (all night times, daytime in spring, winter, and most of autumn), the surface of temperature of TARC is closer to the ideal temperature zone between heating and cooling temperature setpoints (22 °C and 24 °C) than other roof coatings. Therefore, TARC saves more energy than the white roof coating from an all-season, day-and-night perspective.

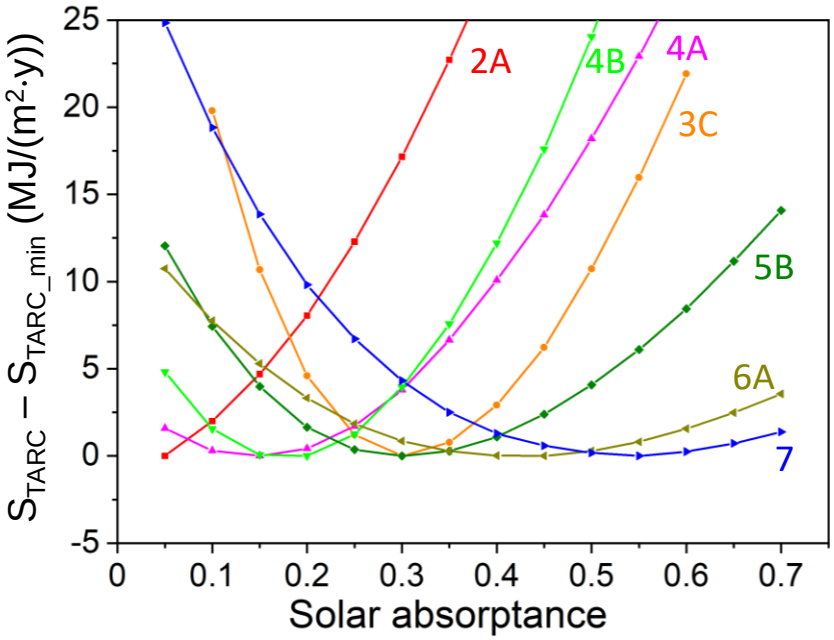

2A: Houston, TX	3C: San Francisco, CA	4A: Baltimore, MD	
4B: Albuquerque, NM	5B: Boise, ID	6A: Burlington, VT	7: Duluth, MN

Figure S7. Calculation of space-conditioning source energy consumption of TARC (S_{TARC}) in different cities as a function of the TARC solar absorptance (A). The indexes (2A, 3C, etc.) represent the different U.S. climate zones. In each curve, S_{TARC} is vertically offset by its minimum value for better display of the data in the plot. Each S_{TARC} curve is U shaped, suggesting that a solar absorptance neither too low nor too high is desirable. The ideal solar absorptance varies depending on the cities, and tends to shift to a higher value for those with colder climates, consistent with expectations. The experimental A of TARC is designed to be approximately 0.25 to 0.30, which is close to the optimal A (minimum point of the curves) for major U.S. cities.

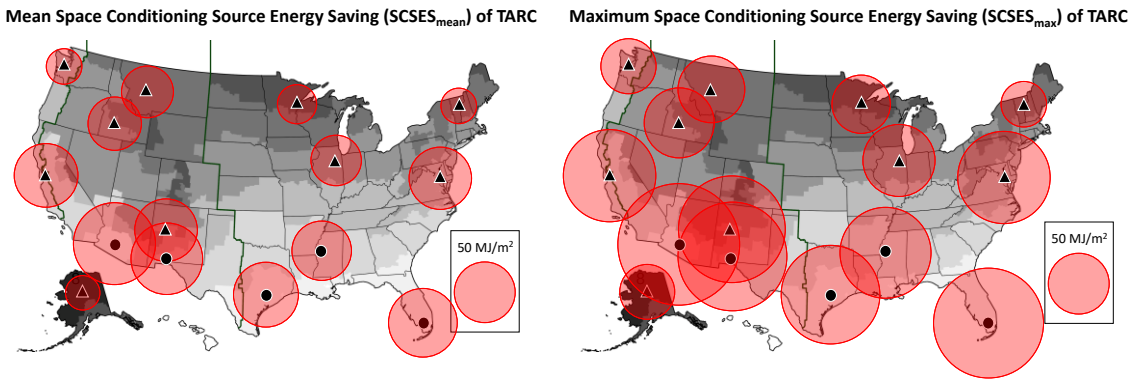

Figure S8. Mean space conditioning source energy saving (SCSES$_{mean}$) and maximum space conditioning source energy saving (SCSES$_{max}$) of TARC. SCSES$_{mean}$ was calculated by averaging SCSEC over all available reference materials; SCSES$_{max}$ is the maximum savings relative to all reference coatings.

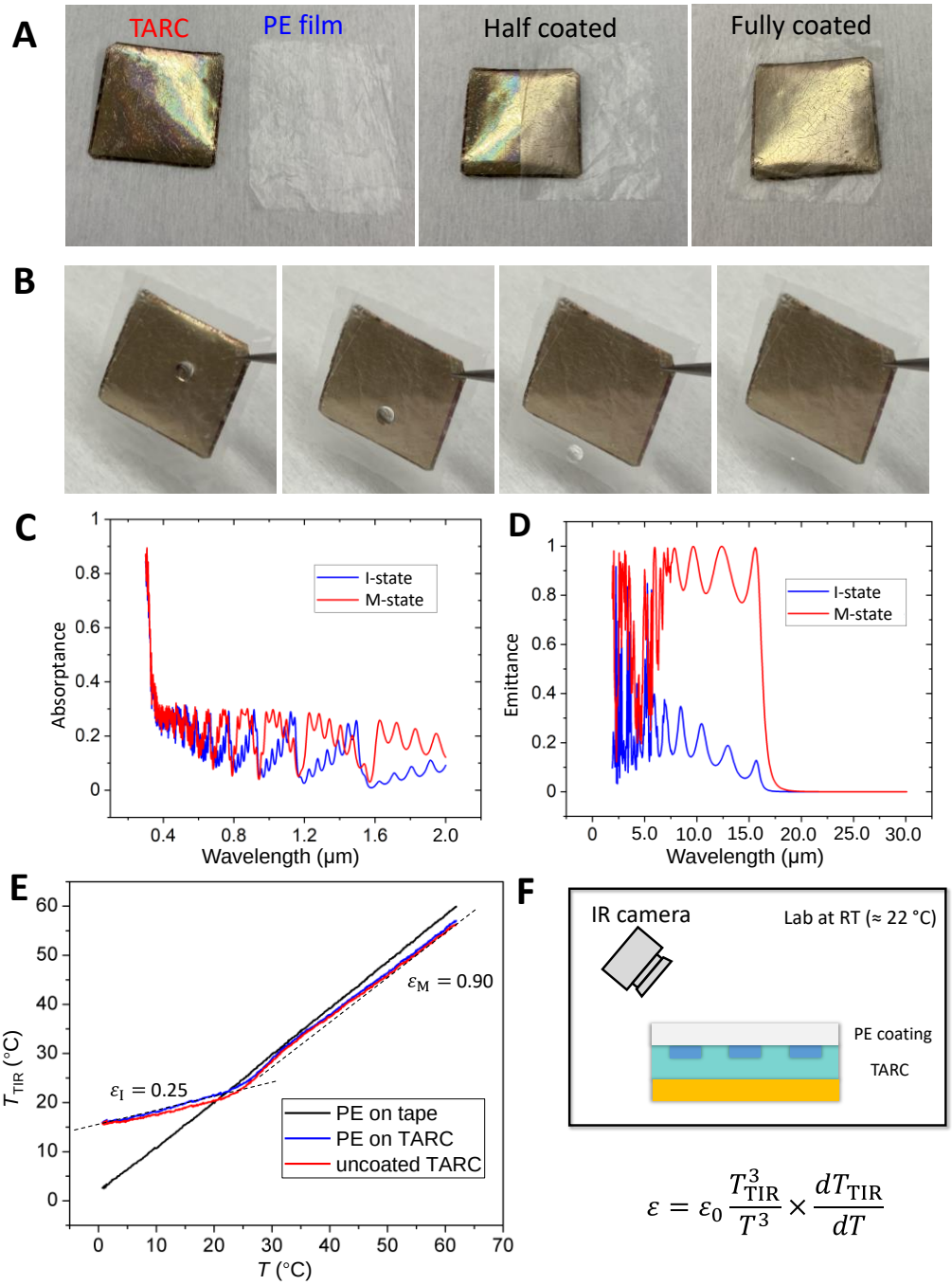

Figure S9. Demonstration of PE-coated TARC for practical applications. A. Photos showing the setup of TARC coated with PE. **B.** Photos showing the hydrophobicity of PE-coated TARC, where water was dropped onto the PE-coated TARC sample. **C-D.** Calculated solar absorptance spectra and IR emittance spectra of TARC covered with PE. **E.** Experimental characterization of thermal emittance for a PE-coated TARC compared to an uncoated sample, showing that the additional PE coating has a negligible influence on the TARC thermal modulation performance. **F.** Schematic for the thermal emittance characterization via IR camera measurement.

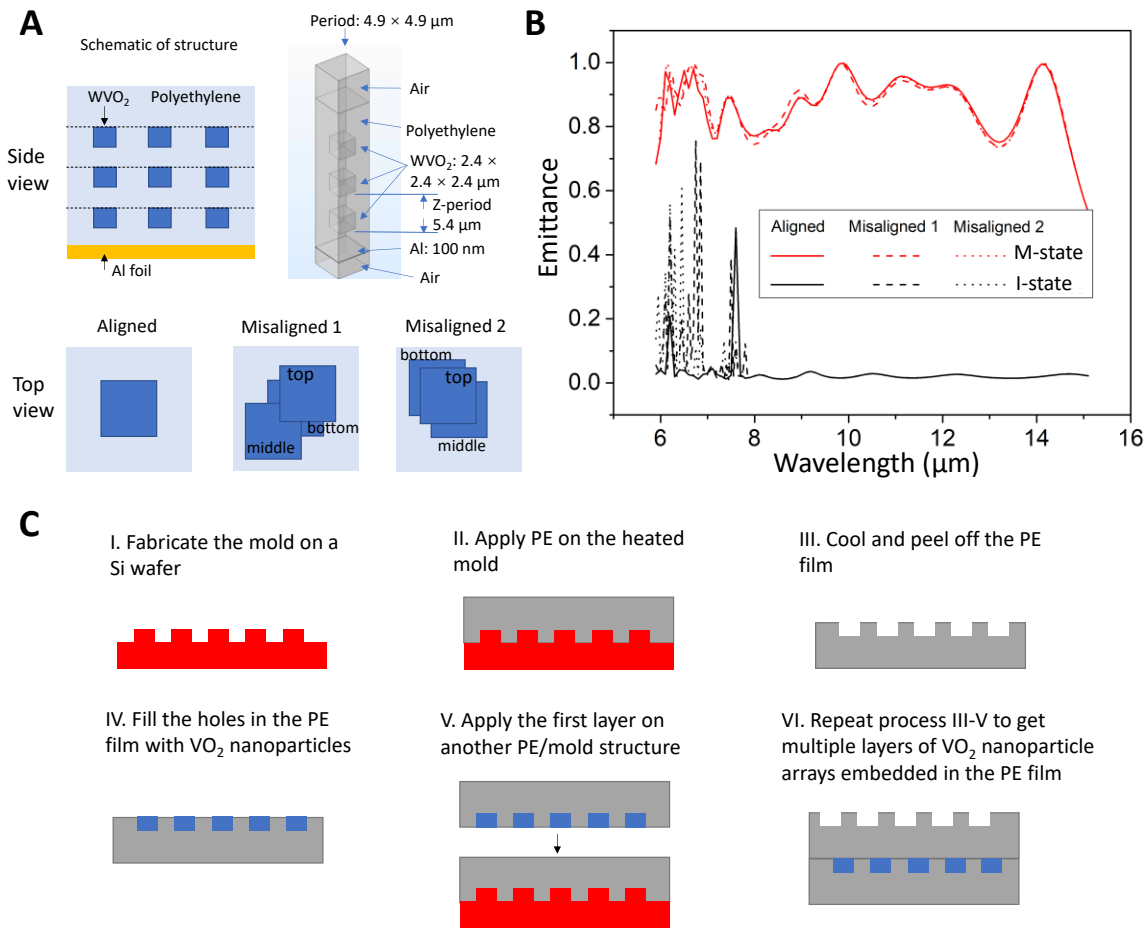

Figure S10. An alternative structural design and processing for mass production of TARC. A. Schematic design of the structure by tri-layer WVO_2 arrays embedded in polyethylene (PE) films. **B.** Spectral emittance of the I state and M state of the PE-based TARC film calculated by COMSOL. Significant emittance modulation ($\Delta\varepsilon_w > 0.8$) is available, which also applies to structures with misaligned WVO_2 blocks in actual scenarios. **C.** Potential fabrication steps of the PE-based TARC film. Mass production is achievable via layer-by-layer nano-imprinting from a pre-fabricated Si wafer mold. Note that the Si wafer mold can be replaced by metallic imprinting mold for mass production in a roll-by-roll fashion.

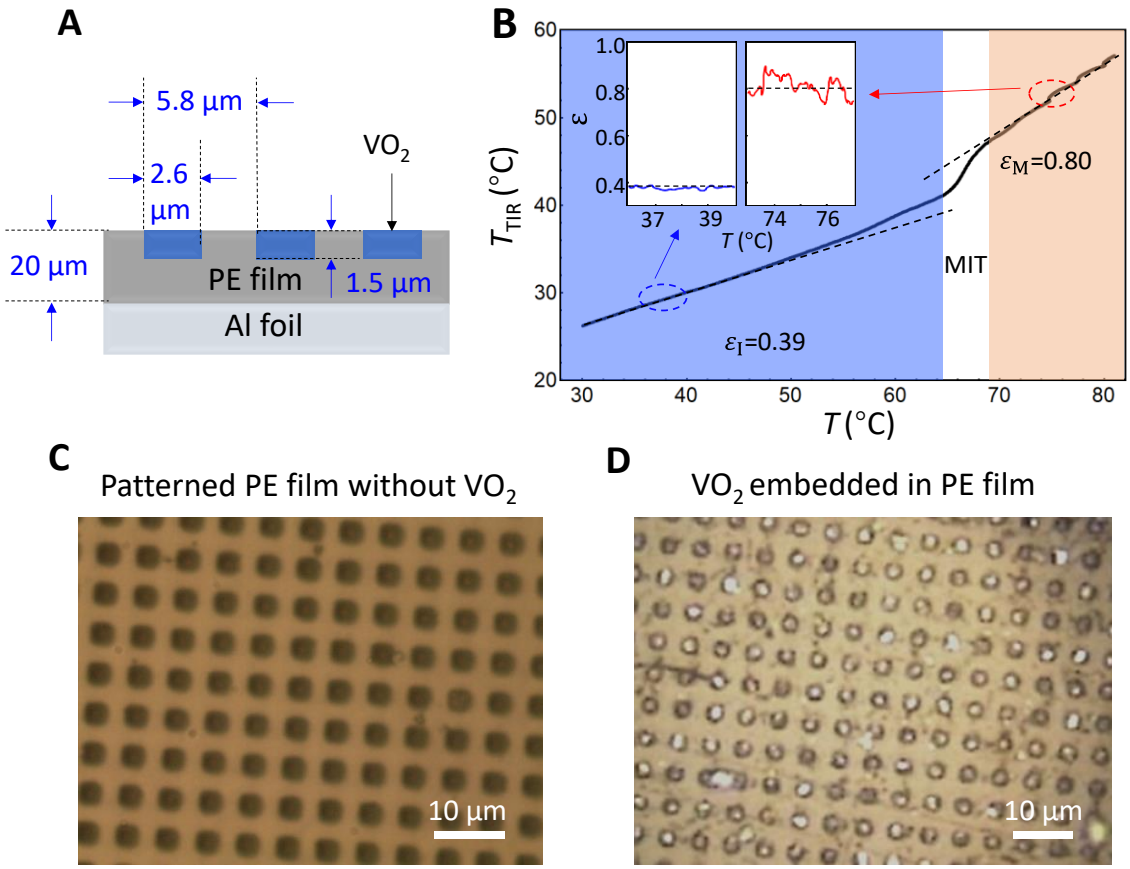

Figure S11. Preliminary results for the mass production of TARC based on the VO_2-embedded-in-PE approach, using only a single layer. The emittance (0.39) when VO_2 is in the I state can be further decreased by using thinner PE films. The emittance (0.80) when VO_2 is in the M state can be raised by stacking several PE-based TARC layers together. As a roof-coating material, PE-based coatings have a typical lifetime ranging from months (*54*) to years (*55*). This can be further prolonged by introducing advanced organic films (*10*,*56*). Furthermore, chemical additives and high-quality barrier coatings can also help optimize the durability of organic coatings (*9*).

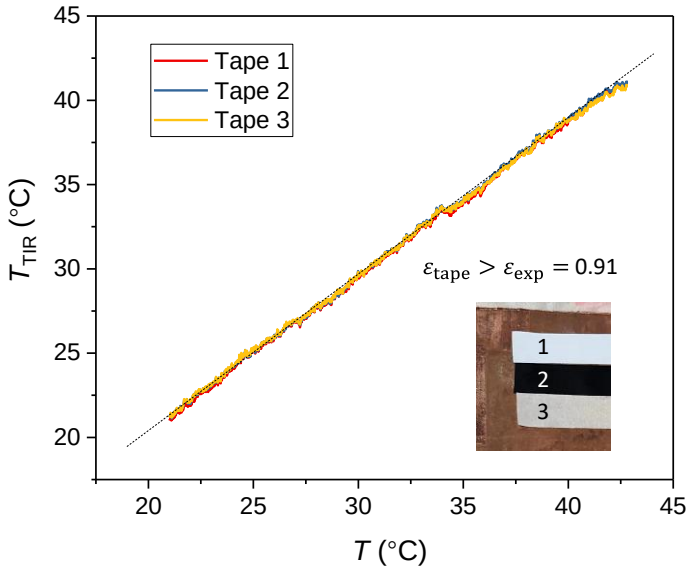

Figure S12. Experimental characterization of thermal emittance of the tape used in the experiments. Three pieces of tape were pasted onto a copper heating plate, and an IR camera (FLIR ONE) was used to measure the thermal IR temperature (T_{TIR}) as a function of the contact temperature (T) measured by a Pt temperature sensor mounted near the tape. The thermal emittance of tape was extracted as 0.91. Due to heat convection and conduction, the tape's true temperature is always slightly lower than its measured contact temperature. Thus, the tape's true thermal emittance ($\varepsilon_{\text{tape}}$) is higher than this extracted experimental thermal emittance (ε_{exp} = 0.91), so the emissivity of tape is assumed to be 0.95 in other experiments according to reference (*57*).

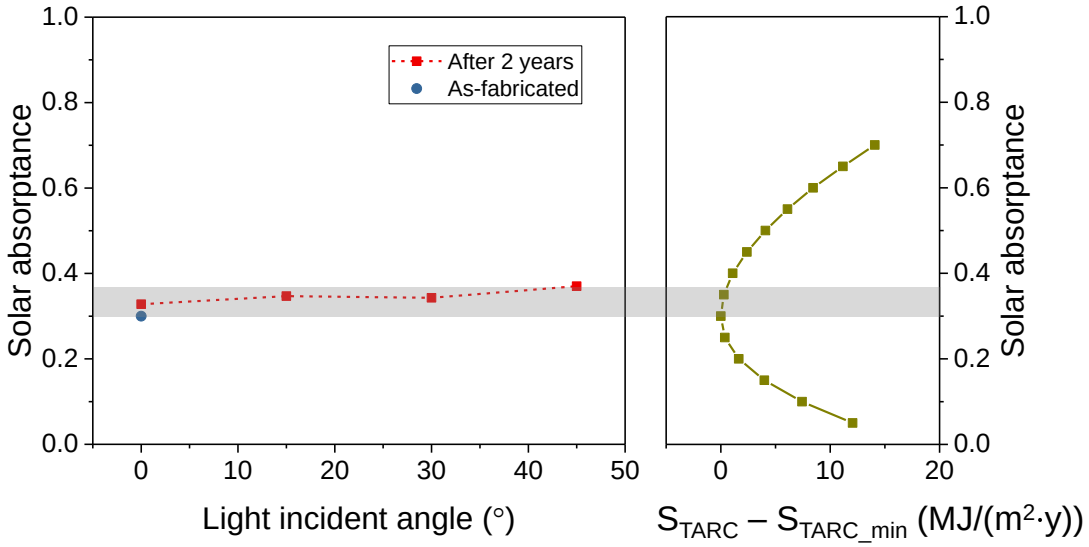

Figure S13. Solar absorptance characterization of TARC at different light incident angles. The experimental details and absorptance extraction method can be found in Fig. S3. The TARC sample has aged for two years before the angle testing. The solar absorptance at normal incidence increases only by 0.03 after the two-year aging. When the light incident angle increases from 0° (normal incidence) to 45°, the solar absorptance of TARC increases only by 0.04. This absorptance variation is compared to the normalized S_{TARC} in Boise, ID (details in Fig. S7), showing that the solar absorptance variation due to aging and light incident angles still falls well within the optimal range of S_{TARC}.

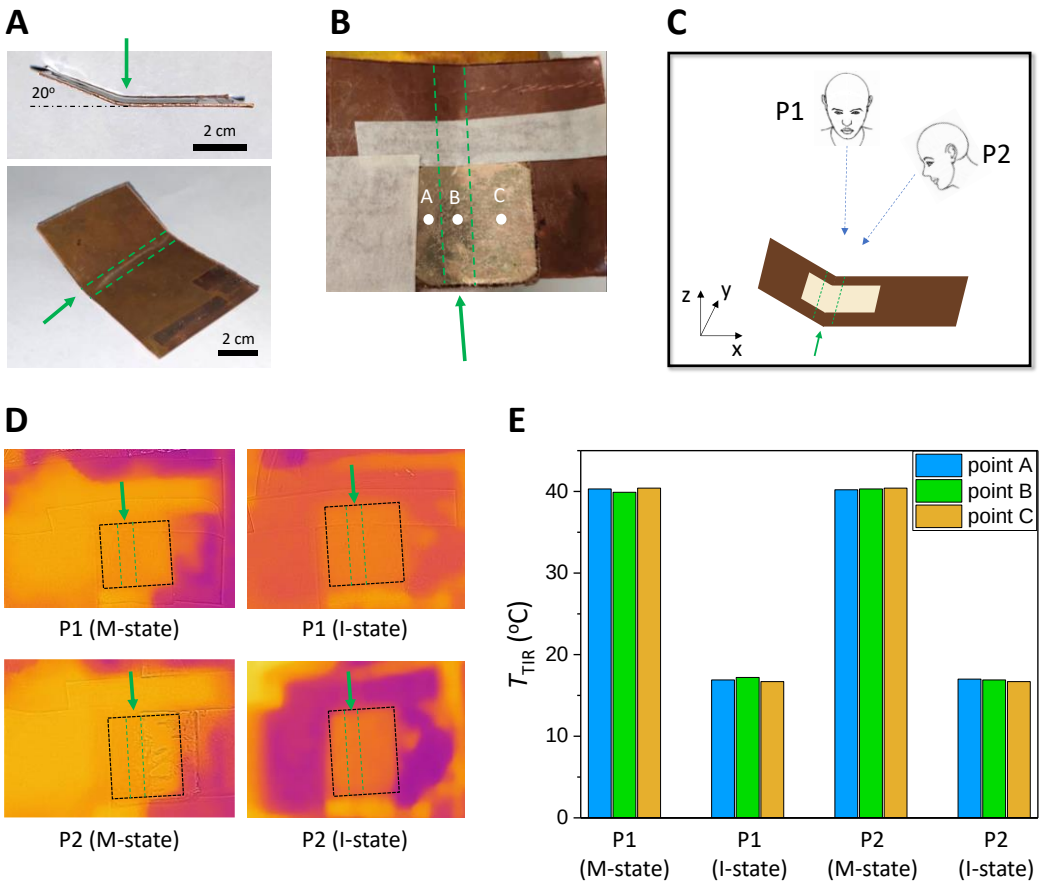

Figure S14. **TIR performance of TARC at different tilting angles and shape deformation**. **A.** Photos of a copper plate with a 20° bend. The bending edge is denoted by a green arrow, and the bending area is marked by two parallel green dashed lines (which are also shown in the other panels). **B.** A TARC was pasted onto the deformed copper plate, covering the bending edge. The three points (A, B, C) mark the positions where thermal IR temperatures (T_{TIR}) are measured in panel E. Two pieces of tape applied next to TARC served as positioning markers in TIR images. **C.** Schematic for the experiment setup, where the default viewing angle of the IR camera (FLIR ONE) was set to 30°. The human-head icons show the IR camera positions and orientations in the YZ-plane (P1) and XZ-plane (P2). **D.** TIR images of the TARC (dashed black box) under different conditions. The copper plate was heated/cooled to about 40 °C/7 °C to test the device performance when WVO_2 is in M state/I state. Note that each TIR image has its individual color scale. **E.** Thermal IR temperature (T_{TIR}) measured at different positions. The homogeneous T_{TIR} across the whole TARC indicate that its emittance is insensitive to both shape deformation and tilting angle.

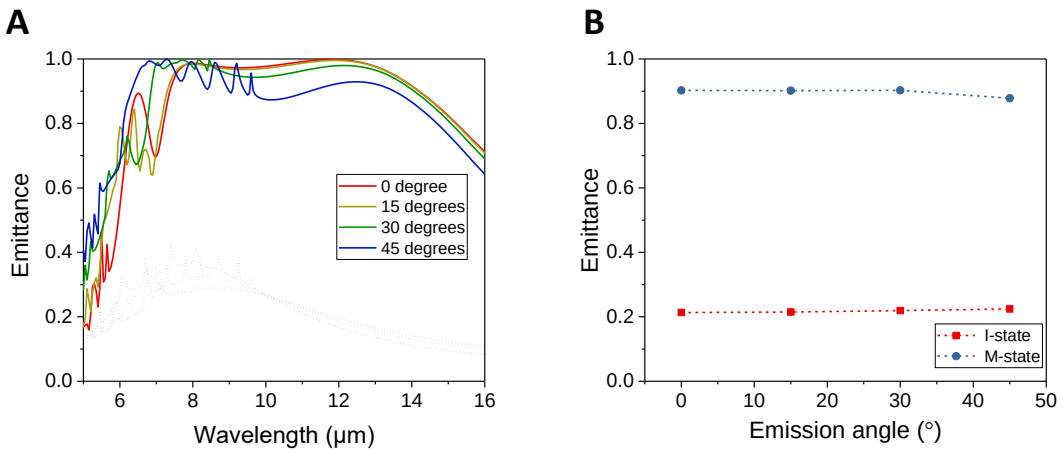

Figure S15. Simulated thermal IR spectral emittance at different emission angles. A. Spectral emittance of TARC at different emission angles. Solid and dotted lines correspond to the cases where the W-doped VO_2 in TARC is in M state and I state, respectively. **B.** Integrated emittance of TARC as a function of emission angles.

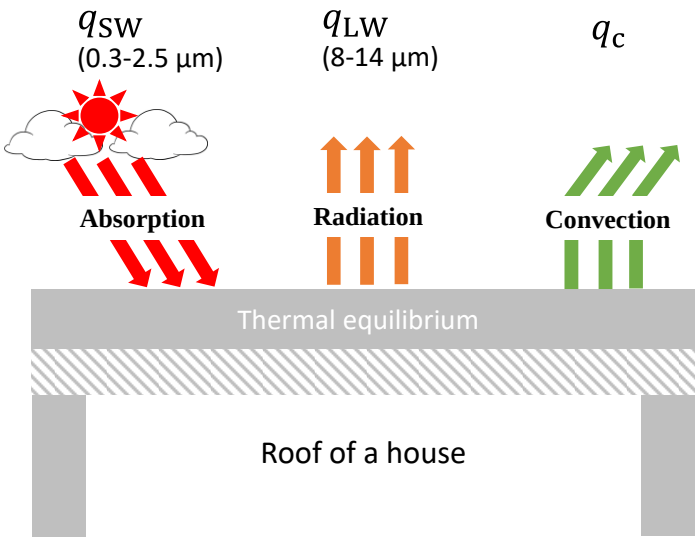

Figure S16. Schematic of the adiabatic approximation for surface temperature calculation. For a surface with given solar absorptance (A) and sky-window thermal emittance (ε_w), this model enables the calculation of the surface temperature T_s in any climate.

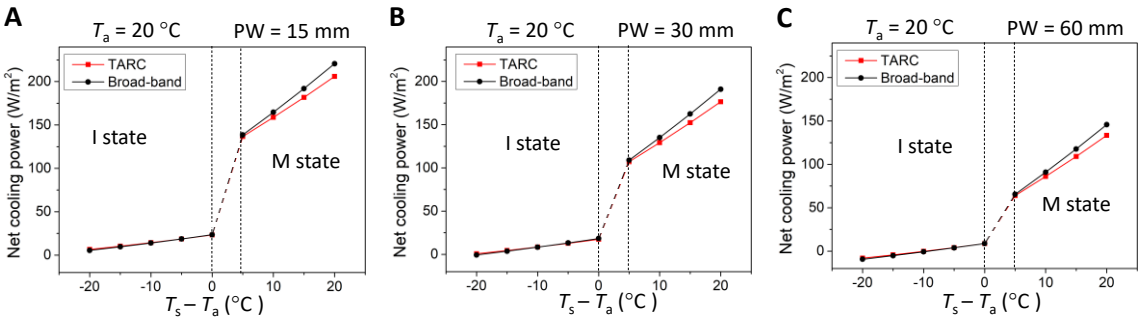

Figure S17. Calculated net radiative cooling power of TARC and a broad-band emitter with a constant emittance equal to ε_w of TARC. The results include conditions with various surface temperatures and precipitable water (PW). The atmospheric spectral emittances for different PW are obtained from (*50*).

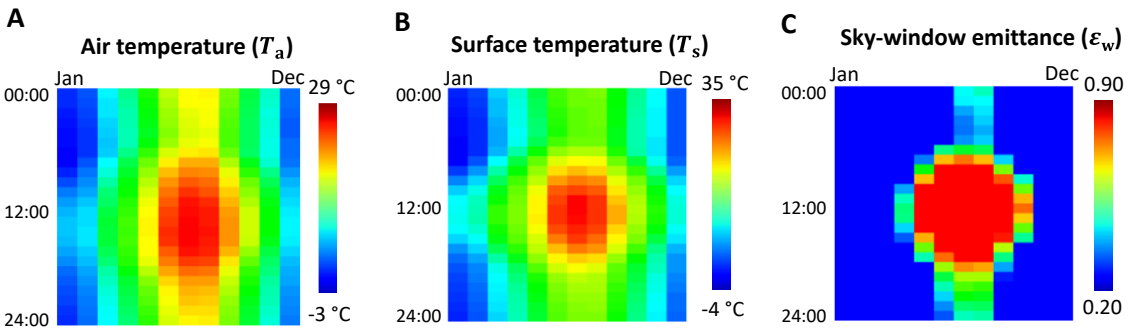

Figure S18. Example of surface temperature calculation based on the model for Baltimore, MD.

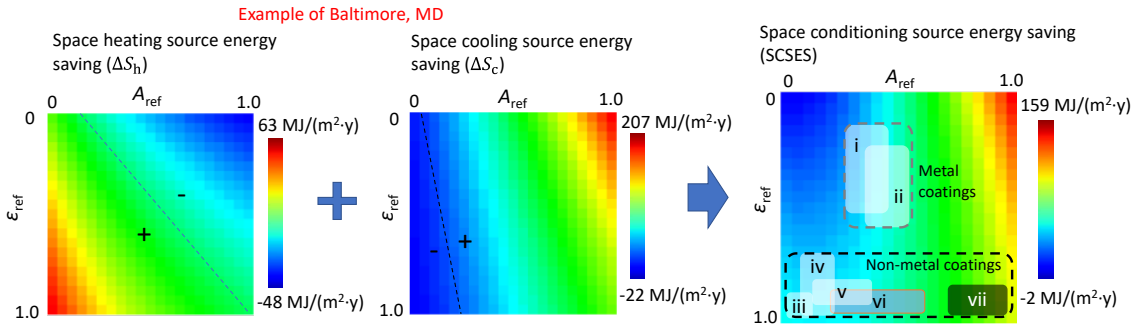

Figure S19. Calculated energy saving advantage of TARC compared with conventional materials. All savings are normalized to roof area. The indexes in the SCSES map represent: i, white metal plate; ii, aluminum pigments; iii, daytime radiative coolers; iv, silicone; v, acrylic; vi, polyurethane; and vii, asphalt.

Supplementary Tables

Table S1. Detailed information for the compared thermal regulation technologies in Fig. 1B with references.

Part A. Energy-consuming devices[a]

Category		Representative power (W)	Index in Fig. 1B	Reference
Peltier cooler		0.3-400	1	58-62
Refrigerator (parts)		20-3,700	2	63-66
Caloric cooling		0.03-3,000	3	67-71
Membrane-assisted cooling		40-22,700	4	72-75
Air conditioner (with heating)	Cooling	2,100-17,600	5	76-82
	Heating	1,100-4,700	6	
Joule heating		70-1,500	7	83-86
Gas heating		2,900-29,400	8	87-90

Part B. Energy-free materials

Category		Representative power (W/m^2)	Index in Fig. 1B	Reference
Daytime radiative cooler[b]	Nanoparticles	70-93	9	9,91
	Wood	16	10	11
	Polymer membranes	20-127	11	8,10,92-94
	Multilayer nanofilms	14-41	12	95,96
	Soft textiles (together with thermal emitters)[c]	60-96	13	39,97
TARC (this work)	Cooling (without sunlight)	0-110	14	This work
	Heating (with sunlight)	0-250	14	
Typical dark roof paint	Heating (with AM1.5 sunlight)	600-980	15	98-100
Standard brick		350-890	16	100-102
Al coating		120-300	17	100-102
Asphalt shingles		650-970	18	103-105

[a] Although most heaters/coolers can adjust their heating/cooling power from zero to the maximum power, in the master plot (Fig. 1B) we only graphed the ranges for the maximum heating/cooling powers.

[b] Only considers the net cooling power under direct sunlight in field experiments—i.e., cooling power minus heating power. Simulation data are not included here. If possible, the surface temperature is set to be ambient temperature.

[c] Soft textiles are usually tested while they are placed on thermal emitters. Details can be found in (*39*,*97*).

Table S2. Regressed coefficients α_h and α_c for single-family homes of different vintages in cities across the U.S. Units: MJ/(m²·y·K), where m² refers to the roof area.

Climate zone	Location	Oldest (pre-1980)		Older (1980-1999)		New	
		α_h	α_c	α_h	α_c	α_h	α_c
1A	Miami, FL	31.48	24.52	21.24	10.55	18.87	8.53
2A	Houston, TX	33.00	22.61	23.30	11.28	19.93	7.67
2B	Phoenix, AZ	22.55	25.56	16.48	10.64	16.23	11.34
3A	Memphis, TN	17.97	23.29	11.77	11.37	11.71	11.25
3B	El Paso, TX	20.94	22.43	17.69	10.57	13.54	7.34
3C	San Francisco, CA	28.75	26.94	21.18	9.87	13.56	6.57
4A	Baltimore, MD	26.36	30.81	13.50	12.21	9.46	7.10
4B	Albuquerque, NM	20.90	27.17	14.64	10.45	13.26	7.72
4C	Seattle, WA	17.85	11.84	11.75	4.98	8.69	3.66
5A	Peoria, IL	18.19	22.76	11.13	10.44	8.85	7.47
5B	Boise, ID	21.86	16.86	12.56	6.55	11.85	4.81
6A	Burlington, VT	13.69	14.50	11.52	8.67	8.97	7.01
6B	Helena, MT	22.47	24.02	11.97	8.98	10.19	5.53
7	Duluth, MN	17.68	19.07	10.91	7.91	8.97	7.18
8	Fairbanks, AK	14.19	15.91	8.67	6.87	8.05	5.67

Table S3. Regressed coefficients α_h and α_c for apartment buildings of different vintages in cities across the U.S. Units: MJ/(m²·y·K), where m² refers to the roof area.

Climate zone	Location	Oldest (pre-1980)		Older (1980-1999)		New	
		α_h	α_c	α_h	α_h	α_c	α_h
1A	Miami, FL	43.99	24.37	28.93	10.34	22.30	7.93
2A	Houston, TX	44.84	21.93	27.89	10.69	22.30	6.67
2B	Phoenix, AZ	39.24	24.59	24.22	9.96	24.26	9.90
3A	Memphis, TN	21.97	22.52	13.55	10.96	12.39	9.79
3B	El Paso, TX	34.66	21.03	23.23	9.95	17.57	6.12
3C	San Francisco, CA	40.35	23.43	24.37	8.45	14.29	5.09
4A	Baltimore, MD	29.82	29.51	14.40	11.72	9.21	5.60
4B	Albuquerque, NM	30.39	25.10	16.81	9.82	14.48	6.25
4C	Seattle, WA	21.17	10.77	12.22	4.48	7.86	3.65
5A	Peoria, IL	20.75	21.85	11.31	9.60	8.29	5.87
5B	Boise, ID	26.55	15.79	13.57	6.11	11.40	3.89
6A	Burlington, VT	14.48	12.37	12.68	9.76	7.87	5.05
6B	Helena, MT	25.71	22.05	12.37	7.67	8.97	3.86
7	Duluth, MN	21.36	20.78	11.44	8.83	8.20	5.61
8	Fairbanks, AK	17.45	15.28	9.55	6.43	7.42	4.53

Table S4. Calculated $SCSES_{min}$ as the first of merit for TARC in cities across the U.S. Units: MJ/(m^2·y), where m^2 refers to the roof area.

Climate zone	Location	Single-family home			Apartment building		
		Oldest (pre-1980)	Older (1980-1999)	New	Oldest (pre-1980)	Older (1980-1999)	New
1A	Miami, FL	-22.5	-6.6	-4.7	-17.5	-3.3	-2.4
2A	Houston, TX	12.4	9.5	8.6	25.1	11.9	7.18
2B	Phoenix, AZ	-2.1	9.7	8.4	24.1	22.3	22.4
3A	Memphis, TN	7.5	8.4	8.4	14.4	11.6	10.4
3B	El Paso, TX	20.2	16.4	11.3	32.7	15.0	9.0
3C	San Francisco, CA	14	4.2	2.8	10.6	2.03	1.8
4A	Baltimore, MD	22.4	8.5	4.9	21.1	8.1	3.7
4B	Albuquerque, NM	31.3	11.4	8.2	28	10.5	6.3
4C	Seattle, WA	3.1	0.83	-0.83	0.33	-2.1	-0.29
5A	Peoria, IL	14.5	5.7	4.6	13.9	5.9	3.45
5B	Boise, ID	15.1	5.6	3.9	13.7	5.0	2.14
6A	Burlington, VT	5.2	2.7	2.6	3.9	2.5	0.54
6B	Helena, MT	11.8	4.0	-0.039	10.0	1.6	-0.81
7	Duluth, MN	4.5	1.4	0.12	3.9	-0.031	-0.99
8	Fairbanks, AK	-1.0	-0.72	-2.7	-3.7	-3.4	-3.0

Table S5. Regressed coefficients β_h and β_c (dimensionless) for single-family homes of different vintages in cities across the U.S.

Climate zone	Location	Oldest (pre-1980)		Older (1980-1999)		New	
		β_h	β_c	β_h	β_c	β_h	β_c
1A	Miami, FL	0.000	0.219	0.000	0.216	0.000	0.282
2A	Houston, TX	0.000	0.243	0.000	0.238	0.000	0.302
2B	Phoenix, AZ	0.078	0.218	0.114	0.207	0.106	0.209
3A	Memphis, TN	0.003	0.277	0.000	0.269	0.000	0.268
3B	El Paso, TX	0.068	0.262	0.074	0.253	0.091	0.299
3C	San Francisco, CA	0.122	0.395	0.124	0.411	0.151	0.395
4A	Baltimore, MD	0.038	0.344	0.026	0.341	0.045	0.385
4B	Albuquerque, NM	0.081	0.323	0.076	0.315	0.082	0.399
4C	Seattle, WA	0.045	0.486	0.040	0.493	0.054	0.507
5A	Peoria, IL	0.025	0.380	0.017	0.375	0.028	0.438
5B	Boise, ID	0.039	0.352	0.035	0.351	0.036	0.440
6A	Burlington, VT	0.030	0.465	0.070	0.213	0.034	0.517
6B	Helena, MT	0.042	0.434	0.040	0.425	0.039	0.538
7	Duluth, MN	0.086	0.211	0.085	0.222	0.057	0.499
8	Fairbanks, AK	0.060	0.215	0.060	0.213	0.060	0.212

Table S6. Regressed coefficients β_h and β_c (dimensionless) for apartment buildings of different vintages in cities across the U.S.

Climate zone	Location	Oldest (pre-1980)		Older (1980-1999)		New	
		β_h	β_c	β_h	β_c	β_h	β_c
1A	Miami, FL	0.000	0.210	0.000	0.186	0.000	0.261
2A	Houston, TX	0.000	0.216	0.000	0.206	0.000	0.264
2B	Phoenix, AZ	0.121	0.207	0.207	0.196	0.205	0.196
3A	Memphis, TN	0.012	0.259	0.051	0.221	0.017	0.239
3B	El Paso, TX	0.075	0.249	0.088	0.237	0.119	0.283
3C	San Francisco, CA	0.115	0.372	0.113	0.349	0.154	0.335
4A	Baltimore, MD	0.033	0.333	0.035	0.297	0.118	0.295
4B	Albuquerque, NM	0.079	0.312	0.079	0.289	0.102	0.353
4C	Seattle, WA	0.043	0.462	0.040	0.416	0.075	0.384
5A	Peoria, IL	0.035	0.348	0.042	0.297	0.089	0.310
5B	Boise, ID	0.038	0.345	0.033	0.324	0.043	0.383
6A	Burlington, VT	0.060	0.345	0.058	0.310	0.072	0.362
6B	Helena, MT	0.044	0.422	0.065	0.305	0.069	0.370
7	Duluth, MN	0.073	0.373	0.073	0.326	0.075	0.419
8	Fairbanks, AK	0.057	0.309	0.061	0.225	0.061	0.224

References and Notes

1. US Energy Information Administration, “Annual Energy Review 2020” (2020); https://www.eia.gov/totalenergy/data/annual/

2. US Energy Information Administration, “2015 Residential Energy Consumption Survey” (2015); https://www.eia.gov/consumption/residential/

3. A. R. Gentle, G. B. Smith, A subambient open roof surface under the mid-summer sun. *Adv. Sci. (Weinh.)* **2**, 1500119 (2015). doi:10.1002/advs.201500119 Medline

4. M. Dong, N. Chen, X. Zhao, S. Fan, Z. Chen, Nighttime radiative cooling in hot and humid climates. *Opt. Express* **27**, 31587–31598 (2019). doi:10.1364/OE.27.031587 Medline

5. B. Orel, M. K. Gunde, A. Krainer, Radiative cooling efficiency of white pigmented paints. *Sol. Energy* **50**, 477–482 (1993). doi:10.1016/0038-092X(93)90108-Z

6. P. Berdahl, M. Martin, F. Sakkal, Thermal performance of radiative cooling panels. *Int. J. Heat Mass Transf.* **26**, 871–880 (1983). doi:10.1016/S0017-9310(83)80111-2

7. N. N. Shi, C.-C. Tsai, F. Camino, G. D. Bernard, N. Yu, R. Wehner, Thermal physiology. Keeping cool: Enhanced optical reflection and radiative heat dissipation in Saharan silver ants. *Science* **349**, 298–301 (2015). doi:10.1126/science.aab3564 Medline

8. J. Kou, Z. Jurado, Z. Chen, S. Fan, A. J. Minnich, Daytime radiative cooling using near-black infrared emitters. *ACS Photonics* **4**, 626–630 (2017). doi:10.1021/acsphotonics.6b00991

9. Y. Zhai, Y. Ma, S. N. David, D. Zhao, R. Lou, G. Tan, R. Yang, X. Yin, Scalable-manufactured randomized glass-polymer hybrid metamaterial for daytime radiative cooling. *Science* **355**, 1062–1066 (2017). doi:10.1126/science.aai7899 Medline

10. J. Mandal, Y. Fu, A. C. Overvig, M. Jia, K. Sun, N. N. Shi, H. Zhou, X. Xiao, N. Yu, Y. Yang, Hierarchically porous polymer coatings for highly efficient passive daytime radiative cooling. *Science* **362**, 315–319 (2018). doi:10.1126/science.aat9513 Medline

11. T. Li, Y. Zhai, S. He, W. Gan, Z. Wei, M. Heidarinejad, D. Dalgo, R. Mi, X. Zhao, J. Song, J. Dai, C. Chen, A. Aili, A. Vellore, A. Martini, R. Yang, J. Srebric, X. Yin, L. Hu, A radiative cooling structural material. *Science* **364**, 760–763 (2019). doi:10.1126/science.aau9101 Medline

12. Z. Li, Q. Chen, Y. Song, B. Zhu, J. Zhu, Fundamentals, materials, and applications for daytime radiative cooling. *Adv. Mater. Technol.* **5**, 1901007 (2020). doi:10.1002/admt.201901007

13. P. Berdahl, Radiative cooling with MgO and/or LiF layers. *Appl. Opt.* **23**, 370–372 (1984). doi:10.1364/AO.23.000370 Medline

14. X. Li, J. Peoples, Z. Huang, Z. Zhao, J. Qiu, X. Ruan, Full daytime sub-ambient radiative cooling in commercial-like paints with high figure of merit. *Cell Rep. Phys. Sci.* **1**, 100221 (2020). doi:10.1016/j.xcrp.2020.100221

15. G. Ulpiani, G. Ranzi, K. W. Shah, J. Feng, M. Santamouris, On the energy modulation of daytime radiative coolers: A review on infrared emissivity dynamic switch against overcooling. *Sol. Energy* **209**, 278–301 (2020). doi:10.1016/j.solener.2020.08.077

16. K. Goncharov, A. Orlov, A. Tarabrin, M. Gottero, V. Perotto, S. Tavera, G. P. Zoppo, “1500 W deployable radiator with loop heat pipe” (SAE Technical Paper 2001-01-2194, 2001); https://doi.org/10.4271/2001-01-2194.

17. C. Lashley, S. Krein, P. Barcomb, “Deployable radiators-A multi-discipline approach” (SAE Technical Paper 981691, 1998); https://doi.org/10.4271/981691.

18. H. Zhao, Q. Sun, J. Zhou, X. Deng, J. Cui, Switchable cavitation in silicone coatings for energy-saving cooling and heating. *Adv. Mater.* **32**, e2000870 (2020). doi:10.1002/adma.202000870 Medline

19. Z. Xia, Z. Fang, Z. Zhang, K. Shi, Z. Meng, Easy way to achieve self-adaptive cooling of passive radiative materials. *ACS Appl. Mater. Interfaces* **12**, 27241–27248 (2020). doi:10.1021/acsami.0c05803 Medline

20. H. Nagano, Y. Nagasaka, A. Ohnishi, Simple deployable radiator with autonomous thermal control function. *J. Thermophys. Heat Trans.* **20**, 856–864 (2006). doi:10.2514/1.17988

21. M. Ono, K. Chen, W. Li, S. Fan, Self-adaptive radiative cooling based on phase change materials. *Opt. Express* **26**, A777–A787 (2018). doi:10.1364/OE.26.00A777 Medline

22. M. Chen, A. M. Morsy, M. L. Povinelli, Design of VO_2-coated silicon microspheres for thermally-regulating paint. *Opt. Express* **27**, 21787–21793 (2019). doi:10.1364/OE.27.021787 Medline

23. S. Taylor, Y. Yang, L. Wang, Vanadium dioxide based Fabry-Perot emitter for dynamic radiative cooling applications. *J. Quant. Spectrosc. Radiat. Transf.* **197**, 76–83 (2017). doi:10.1016/j.jqsrt.2017.01.014

24. W.-W. Zhang, H. Qi, A.-T. Sun, Y.-T. Ren, J.-W. Shi, Periodic trapezoidal VO_2-Ge multilayer absorber for dynamic radiative cooling. *Opt. Express* **28**, 20609–20623 (2020). doi:10.1364/OE.396171 Medline

25. K. Ito, T. Watari, K. Nishikawa, H. Yoshimoto, H. Iizuka, Inverting the thermal radiative contrast of vanadium dioxide by metasurfaces based on localized gap-plasmons. *APL Photonics* **3**, 086101 (2018). doi:10.1063/1.5025947

26. K. Nishikawa, K. Yatsugi, Y. Kishida, K. Ito, Temperature-selective emitter. *Appl. Phys. Lett.* **114**, 211104 (2019). doi:10.1063/1.5091048

27. H. Kim, K. Cheung, R. C. Y. Auyeung, D. E. Wilson, K. M. Charipar, A. Piqué, N. A. Charipar, VO_2-based switchable radiator for spacecraft thermal control. *Sci. Rep.* **9**, 11329 (2019). doi:10.1038/s41598-019-47572-z Medline

28. K. Sun, C. A. Riedel, A. Urbani, M. Simeoni, S. Mengali, M. Zalkovskij, B. Bilenberg, C. H. de Groot, O. L. Muskens, VO_2 thermochromic metamaterial-based smart optical solar reflector. *ACS Photonics* **5**, 2280–2286 (2018). doi:10.1021/acsphotonics.8b00119

29. X. Xue, M. Qiu, Y. Li, Q. M. Zhang, S. Li, Z. Yang, C. Feng, W. Zhang, J.-G. Dai, D. Lei, W. Jin, L. Xu, T. Zhang, J. Qin, H. Wang, S. Fan, Creating an eco-friendly building coating with smart subambient radiative cooling. *Adv. Mater.* **32**, e1906751 (2020). doi:10.1002/adma.201906751 Medline

30. F. J. Morin, Oxides which show a metal-to-insulator transition at the neel temperature. *Phys. Rev. Lett.* **3**, 34–36 (1959). doi:10.1103/PhysRevLett.3.34

31. T.-L. Wu, L. Whittaker, S. Banerjee, G. Sambandamurthy, Temperature and voltage driven tunable metal-insulator transition in individual $W_xV_{1-x}O_2$ nanowires. *Phys. Rev. B Condens. Matter Mater. Phys.* **83**, 073101 (2011). doi:10.1103/PhysRevB.83.073101

32. C. Kim, J. S. Shin, H. Ozaki, Effect of W doping in metal–insulator transition material VO_2 by tunnelling spectroscopy. *J. Phys. Condens. Matter* **19**, 096007 (2007). doi:10.1088/0953-8984/19/9/096007

33. S. Lee, K. Hippalgaonkar, F. Yang, J. Hong, C. Ko, J. Suh, K. Liu, K. Wang, J. J. Urban, X. Zhang, C. Dames, S. A. Hartnoll, O. Delaire, J. Wu, Anomalously low electronic thermal conductivity in metallic vanadium dioxide. *Science* **355**, 371–374 (2017). doi:10.1126/science.aag0410 Medline

34. A. S. Barker, H. W. Verleur, H. J. Guggenheim, Infrared optical properties of vanadium dioxide above and below the transition temperature. *Phys. Rev. Lett.* **17**, 1286–1289 (1966). doi:10.1103/PhysRevLett.17.1286

35. J. Agassi, The kirchhoff-planck radiation law. *Science* **156**, 30–37 (1967). doi:10.1126/science.156.3771.30 Medline

36. The materials and methods are available as supplementary materials.

37. US Department of Energy, "EnergyPlus Weather Data" (2021); https://energyplus.net/weather.

38. P. J. Rosado, R. Levinson, Potential benefits of cool walls on residential and commercial buildings across California and the United States: Conserving energy, saving money, and reducing emission of greenhouse gases and air pollutants. *Energy Build.* **199**, 588–607 (2019). doi:10.1016/j.enbuild.2019.02.028

39. A. Leroy, B. Bhatia, C. C. Kelsall, A. Castillejo-Cuberos, M. Di Capua H, L. Zhao, L. Zhang, A. M. Guzman, E. N. Wang, High-performance subambient radiative cooling enabled by optically selective and thermally insulating polyethylene aerogel. *Sci. Adv.* **5**, eaat9480 (2019). doi:10.1126/sciadv.aat9480 Medline

40. M. A. Ordal, R. J. Bell, R. W. Alexander Jr., L. L. Long, M. R. Querry, Optical properties of fourteen metals in the infrared and far infrared: Al, Co, Cu, Au, Fe, Pb, Mo, Ni, Pd, Pt, Ag, Ti, V, and W. *Appl. Opt.* **24**, 4493–4499 (1985). doi:10.1364/AO.24.004493 Medline

41. K. Dong, S. Hong, Y. Deng, H. Ma, J. Li, X. Wang, J. Yeo, L. Wang, S. Lou, K. B. Tom, K. Liu, Z. You, Y. Wei, C. P. Grigoropoulos, J. Yao, J. Wu, A lithography-free and field-programmable photonic metacanvas. *Adv. Mater.* **30**, 1703878 (2018). doi:10.1002/adma.201703878 Medline

42. M. M. Qazilbash, M. Brehm, G. O. Andreev, A. Frenzel, P. C. Ho, B.-G. Chae, B.-J. Kim, S. J. Yun, H.-T. Kim, A. V. Balatsky, O. G. Shpyrko, M. B. Maple, F. Keilmann, D. N. Basov, Infrared spectroscopy and nano-imaging of the insulator-to-metal transition in vanadium dioxide. *Phys. Rev. B Condens. Matter Mater. Phys.* **79**, 075107 (2009). doi:10.1103/PhysRevB.79.075107

43. M. R. Querry, “Optical constants of minerals and other materials from the millimeter to the ultraviolet” (US Army Report CRDECCR-88009, 1987); https://apps.dtic.mil/sti/pdfs/ADA192210.pdf.

44. P. B. Johnson, R. W. Christy, Optical constants of the noble metals. *Phys. Rev., B, Solid State* **6**, 4370–4379 (1972). doi:10.1103/PhysRevB.6.4370

45. J. B. Kana Kana, G. Vignaud, A. Gibaud, M. Maaza, Thermally driven sign switch of static dielectric constant of VO_2 thin film. *Opt. Mater.* **54**, 165–169 (2016). doi:10.1016/j.optmat.2016.02.032

46. I. H. Malitson, Refractive properties of barium fluoride. *J. Opt. Soc. Am.* **54**, 628–632 (1964). doi:10.1364/JOSA.54.000628

47. T. L. Bergman, F. P. Incropera, D. P. DeWitt, A. S. Lavine, “Radiation exchange between surfaces,” in *Fundamentals of Heat and Mass Transfer*, F. P. Incropera, D. P. DeWitt, T. L. Bergman, A. S. Lavine, Eds. (Wiley, ed. 6, 2005), pp. 832–833.

48. Energy Information Administration, “Forms EIA-457A and EIA-457C of the 2015 Residential Energy Consumption Survey, Table HC2.1: Structural and geographic characteristics of US homes by housing unit type” (2015); https://www.eia.gov/consumption/residential/data/2015/hc/php/hc2.1.php.

49. Y. Qin, J. E. Hiller, Ways of formulating wind speed in heat convection significantly influencing pavement temperature prediction. *Heat Mass Transf.* **49**, 745–752 (2013). doi:10.1007/s00231-013-1116-0

50. D. Zhao, A. Aili, Y. Zhai, S. Xu, G. Tan, X. Yin, R. Yang, Radiative sky cooling: Fundamental principles, materials, and applications. *Appl. Phys. Rev.* **6**, 021306 (2019). doi:10.1063/1.5087281

51. L. M. Jiji, *Heat Convection* (Springer, 2009).

52. R. Tang, Y. Etzion, I. A. Meir, Estimates of clear night sky emissivity in the Negev Highlands, Israel. *Energy Convers. Manage.* **45**, 1831–1843 (2004). doi:10.1016/j.enconman.2003.09.033

53. A. Skartveit, J. A. Olseth, G. Czeplak, M. Rommel, On the estimation of atmospheric radiation from surface meteorological data. *Sol. Energy* **56**, 349–359 (1996). doi:10.1016/0038-092X(95)00117-A

54. B. Youssef, A. E. Dehbi, A. Hamou, J. M. Saiter, Natural ageing of tri-layer polyethylene film: Evolution of properties and lifetime in North Africa region. *Mater. Des.* **29**, 2017–2022 (2008). doi:10.1016/j.matdes.2008.04.007

55. A. R. Gentle, K. L. Dybdal, G. B. Smith, Polymeric mesh for durable infra-red transparent convection shields: Applications in cool roofs and sky cooling. *Sol. Energy Mater. Sol. Cells* **115**, 79–85 (2013). doi:10.1016/j.solmat.2013.03.001

56. J. Zhang, Z. Zhou, H. Tang, J. Xing, J. Quan, J. Liu, J. Yu, M. Hu, Mechanically robust and spectrally selective convection shield for daytime subambient radiative cooling. *ACS Appl. Mater. Interfaces* **13**, 14132–14140 (2021). doi:10.1021/acsami.0c21204 Medline

57. S. Wang, G. Liu, P. Hu, Y. Zhou, Y. Ke, C. Li, J. Chen, T. Cao, Y. Long, Largely lowered transition temperature of a VO_2/carbon hybrid phase change material with high thermal emissivity switching ability and near infrared regulations. *Adv. Mater. Interfaces* **5**, 1801063 (2018). doi:10.1002/admi.201801063

58. L. E. Bell, Cooling, heating, generating power, and recovering waste heat with thermoelectric systems. *Science* **321**, 1457–1461 (2008). doi:10.1126/science.1158899 Medline

59. Laird Thermal Systems, "Portfolio Map for thermoelectric coolers of Laird Thermal Systems"; https://www.lairdthermal.com/products/thermoelectric-cooler-modules.

60. II-VI Incorporated, "Product details for Single Stage TEC (Thermoelectric Coolers)"; https://ii-vi.com/product/single-stage-thermoelectric-coolers/.

61. T. E. Technology, Inc., "Cooling power for standard modules"; https://tetech.com/peltier-thermoelectric-cooler-modules/standard/.

62. D. Zhao, G. Tan, A review of thermoelectric cooling: Materials, modeling and applications. *Appl. Therm. Eng.* **66**, 15–24 (2014). doi:10.1016/j.applthermaleng.2014.01.074

63. M. Kassai, L. Kajtar, J. Nyers, Experimental optimization of energy consumption for direct current refrigerator by PID controller tuning and comparison with ON/OFF refrigerator. *Therm. Sci.* **23** (2 Part B), 941–952 (2019). doi:10.2298/TSCI170504188K

64. T. O. Babarinde, S. A. Akinlabi, D. M. Madyira, Energy performance evaluation of R600a/MWCNT-nanolubricant as a drop-in replacement for R134a in household refrigerator system. *Energy Rep.* **6**, 639–647 (2020). doi:10.1016/j.egyr.2019.11.132

65. Y. Jeon, D. Kim, J. Jung, D. S. Jang, Y. Kim, Comparative performance evaluation of conventional and condenser outlet split ejector-based domestic refrigerator-freezers using R600a. *Energy* **161**, 1085–1095 (2018). doi:10.1016/j.energy.2018.08.007

66. Embraco. "Compressor ASPERA NJ9226GK | NJ 9226 GK"; https://elgracool.pl/product-eng-408-Compressor-ASPERA-NJ9226GK-NJ-9226-GK.html.

67. C. R. H. Bahl, K. Engelbrecht, D. Eriksen, J. A. Lozano, R. Bjørk, J. Geyti, K. K. Nielsen, A. Smith, N. Pryds, Development and experimental results from a 1 kW prototype AMR. *Int. J. Refrig.* **37**, 78–83 (2014). doi:10.1016/j.ijrefrig.2013.09.001

68. S. Jacobs, J. Auringer, A. Boeder, J. Chell, L. Komorowski, J. Leonard, S. Russek, C. Zimm, The performance of a large-scale rotary magnetic refrigerator. *Int. J. Refrig.* **37**, 84–91 (2014). doi:10.1016/j.ijrefrig.2013.09.025

69. A. Torelló, P. Lheritier, T. Usui, Y. Nouchokgwe, M. Gérard, O. Bouton, S. Hirose, E. Defay, Giant temperature span in electrocaloric regenerator. *Science* **370**, 125–129 (2020). doi:10.1126/science.abb8045 Medline

70. Y. D. Wang, S. J. Smullin, M. J. Sheridan, Q. Wang, C. Eldershaw, D. E. Schwartza, A heat-switch-based electrocaloric cooler. *Appl. Phys. Lett.* **107**, 134103 (2015). doi:10.1063/1.4932164

71. F. Bruederlin, H. Ossmer, F. Wendler, S. Miyazaki, M. Koh, SMA foil-based elastocaloric cooling: From material behavior to device engineering. *J. Phys. D Appl. Phys.* **50**, 424003 (2017). doi:10.1088/1361-6463/aa87a2

72. M. Alipanah, S. Moghaddam, Ultra-low pressure drop membrane-based heat sink with 1000 W/cm2 cooling capacity and 100% exit vapor quality. *Int. J. Heat Mass Transf.* **161**, 120312 (2020). doi:10.1016/j.ijheatmasstransfer.2020.120312

73. J. Lina, S.-M. Huang, R. Wangc, K. J. Chua, Thermodynamic analysis of a hybrid membrane liquid desiccant dehumidification and dew point evaporative cooling system. *Energy Convers. Manage.* **156**, 440–458 (2018). doi:10.1016/j.enconman.2017.11.057

74. A. H. Abdel-Salam, G. Ge, C. J. Simonson, Performance analysis of a membrane liquid desiccant air-conditioning system. *Energy Build.* **62**, 559–569 (2013). doi:10.1016/j.enbuild.2013.03.028

75. Z. Chen, J. Zhu, H. Bai, Y. Yan, L. Zhang, Experimental study of a membrane-based dehumidification cooling system. *Appl. Therm. Eng.* **115**, 1315–1321 (2017). doi:10.1016/j.applthermaleng.2016.10.153

76. US Department of Energy Office of Energy Saver, "Room air conditioners" (2021); https://www.energy.gov/energysaver/room-air-conditioners.

77. FurnaceCompare, "Cooling capacity" (2019); https://www.furnacecompare.com/faq/definitions/cooling_capacity/.

78. LG Electronics, "Cooling capacity of LG LW8016HR 7,500 BTU Window Air Conditioner, Cooling & Heating"; https://www.lg.com/us/air-conditioners/lg-LW8016HR.

79. LG Electronics, "Cooling capacity of LG LW2416HR 23,000 BTU Window Air Conditioner, Cooling & Heating"; https://www.lg.com/us/air-conditioners/lg-LW2416HR.

80. Haier Group, "Haier 13,500 BTU Portable Air Conditioner AC Unit with Heat Option"; https://www.walmart.com/ip/Haier-13-500-BTU-Portable-Air-Conditioner-AC-Unit-with-Heat-Option-HPND14XHT/129472413.

81. Frigidaire Appliance Company, "Frigidaire 25,000 BTU 230V Heavy-Duty Slide-Out Chassis Air Conditioner with 16,000 BTU Supplemental Heat Capability"; https://www.walmart.com/ip/Frigidaire-25-000-BTU-230V-Heavy-Duty-Slide-Out-Chassis-Air-Conditioner-with-16-000-BTU-Supplemental-Heat-Capability/44458304.

82. General Electric Company, "GE 5,000 BTU 115-Volt Window Air Conditioner with Remote, AHW05LZ, White"; https://www.walmart.com/ip/GE-5-000-BTU-115-Volt-Window-Air-Conditioner-with-Remote-AHW05LZ-White/719358786.

83. General Electric Company, "Power of GE® Portable Heater"; https://www.geappliances.com/appliance/GE-Portable-Heater-ACSK15AK.

84. Lasko Products, "Power of MyHeat™ Personal Heater – Black"; https://www.lasko.com/products/my-heat-personal-heater-black-100/.

85. Cozy Products, "Power of Cozy Toes™ heated carpet mat"; https://www.cozyproducts.com/products/cozy-toes.

86. Honeywell International, "Honeywell Slim Ceramic Tower Heater"; https://www.amazon.com/Honeywell-Ceramic-Tower-Heater-Black/dp/B076CX2QC3.

87. G. H. P. Group, “Thermostatic 30,000 BTU Infrared Vent Free Dual Fuel Wall Heater”; https://www.homedepot.com/p/Dyna-Glo-Thermostatic-30-000-BTU-Infrared-Vent-Free-Dual-Fuel-Wall-Heater-IR30DTDG-2/312915939.

88. Enerco Group, “MR. HEATER Vent-Free 10,000 BTU Radiant Natural Gas”; https://www.zoro.com/mr-heater-vent-free-10-000-btu-radiant-natural-gas-mhvfr10-ng/i/G6237955/.

89. G. H. P. Group, “20,000 BTU Blue Flame Vent Free Natural Gas Thermostatic Wall Heater”; https://www.homedepot.com/p/Dyna-Glo-20-000-BTU-Blue-Flame-Vent-Free-Natural-Gas-Thermostatic-Wall-Heater-BFSS20NGT-4N/310301030.

90. Enerco Group, “HeatStar 100,000 BTU Convection Industrial Portable Natural Gas Heaters”; https://www.mutualscrew.com/product/heatstar-100000-btu-convection-industrial-portable-natural-gas-heaters-239876.cfm.

91. J. Jaramillo-Fernandez, G. L. Whitworth, J. A. Pariente, A. Blanco, P. D. Garcia, C. Lopez, C. M. Sotomayor-Torres, A self-assembled 2D thermofunctional material for radiative cooling. *Small* **15**, e1905290 (2019). doi:10.1002/smll.201905290 Medline

92. L. Zhou, H. Song, J. Liang, M. Singer, M. Zhou, E. Stegenburgs, N. Zhang, C. Xu, T. Ng, Z. Yu, B. Ooi, Q. Gan, A polydimethylsiloxane-coated metal structure for all-day radiative cooling. *Nat. Sustain.* **2**, 718–724 (2019). doi:10.1038/s41893-019-0348-5

93. B. Bartoli, S. Catalanotti, B. Coluzzi, V. Silvestrini, G. Troise, Nocturnal and diurnal performances of selective radiators. *Appl. Energy* **3**, 267–286 (1977). doi:10.1016/0306-2619(77)90015-0

94. H. Zhong, P. Zhang, Y. Li, X. Yang, Y. Zhao, Z. Wang, Highly solar-reflective structures for daytime radiative cooling under high humidity. *ACS Appl. Mater. Interfaces* **12**, 51409–51417 (2020). doi:10.1021/acsami.0c14075 Medline

95. A. P. Raman, M. A. Anoma, L. Zhu, E. Rephaeli, S. Fan, Passive radiative cooling below ambient air temperature under direct sunlight. *Nature* **515**, 540–544 (2014). doi:10.1038/nature13883 Medline

96. S. Y. Jeong, C. Y. Tso, J. Ha, Y. M. Wong, C. Y. H. Chao, B. Huang, H. Qiu, Field investigation of a photonic multi-layered TiO_2 passive radiative cooler in sub-tropical climate. *Renew. Energy* **146**, 44–55 (2020). doi:10.1016/j.renene.2019.06.119

97. L. Cai, A. Y. Song, W. Li, P.-C. Hsu, D. Lin, P. B. Catrysse, Y. Liu, Y. Peng, J. Chen, H. Wang, J. Xu, A. Yang, S. Fan, Y. Cui, Spectrally selective nanocomposite textile for outdoor personal cooling. *Adv. Mater.* **30**, e1802152 (2018). doi:10.1002/adma.201802152 Medline

98. B. Urban, K. Roth, “Guidelines for Selecting Cool Roofs” (US Department of Energy, Office of Energy Efficiency & Renewable Energy, 2010); https://www1.eere.energy.gov/buildings/publications/pdfs/corporate/coolroofguide.pdf.

99. Australian Building Codes Board, “Solar absorption of dark roof colour by National Construction Code (NCC)”; http://steel.com.au/products/coated-steel/colorbond-steel/basix-and-bca-classification.

100. E. I. Griggs, G. E. Courville, “Changes in the heating and cooling energy use in buildings due to lowering the surface solar absorptance of roofs” (US Department of Energy Office of Scientific and Technical Information, 2010); https://www.osti.gov/biblio/6367315.

101. The Engineering ToolBox, “Absorbed solar radiation: Solar radiation absorbed by various materials” (2009); https://www.engineeringtoolbox.com/solar-radiation-absorbed-materials-d_1568.html.

102. V. C. Sharma, A. Sharma, Solar properties of some building elements. *Energy* **14**, 805–810 (1989). doi:10.1016/0360-5442(89)90034-0

103. P. Berdahl, S. E. Bretz, Preliminary survey of the solar reflectance of cool roofing materials. *Energy Build.* **25**, 149–158 (1997). doi:10.1016/S0378-7788(96)01004-3

104. P. Berdahl, H. Akbari, R. Levinson, J. Jacobs, F. Klink, R. Everman, Three-year weathering tests on asphalt shingles: Solar reflectance. *Sol. Energy Mater. Sol. Cells* **99**, 277–281 (2012). doi:10.1016/j.solmat.2011.12.010

105. P. Berdahl, H. Akbari, J. Jacobs, F. Klink, Surface roughness effects on the solar reflectance of cool asphalt shingles. *Sol. Energy Mater. Sol. Cells* **92**, 482–489 (2008). doi:10.1016/j.solmat.2007.10.011